



POLITECNICO DI TORINO

Master Degree in Electronic Engineering

Master Degree Thesis

**Acceleration of Measurement of
Array Antennas Using Inverse
Source Techniques and Information
on a Single Radiating Element**

Supervisor
prof. Giuseppe Vecchi

Candidate
Ettore BARTOLI
277157

Internship Tutor
LINKS Foundation
dott. ing. Marco Righero

ACADEMIC YEAR 2021-2022

Abstract

In most current professional indoor antenna measurement systems, the far-field distance is often too large for a practical shielded and anechoic chamber; hence, the measurement is done in the near field region, and the collected data computationally processed to yield the desired far field pattern; this process is called the "Near-Field to Far-Field transformation". The cost of a measurement is proportional to the number of samples to be measured; the minimum number of necessary samples is ruled by a result equivalent to the sampling theorem for signals, and usually called the Nyquist limit.

In this work, the number of necessary near-field samples is reduced beyond the Nyquist limit by adding information on the geometry of the antenna under test (AUT), and by simulations of parts of the AUT.

This endeavor is made specific for an array antenna, composed of several (nearly) identical antennas interconnected by a network called beam-forming network. The approach is based on the equivalence theorem and on a technique called inverse source; the latter yields the fields on a given source from field samples measured outwards. The on-surface fields on individual antennas (called equivalent currents) are used as basic building blocks to describe the far-field radiation.

The relative reconstruction error with respect to the reference and different methods are discussed.

Summary

Fast antenna measurement has been very popular in the last decade. New progress in communication systems requires more complex antenna designs that imply increasing manufacturing and testing stages during which many sources of error can affect the antennas final prototype, degrading its overall performance and then it requires new design steps to detect and fix these manufacturing errors. This work of thesis aims to reduce the number of sampling points needed for antenna testing below the Nyquist limit by integrating the missing information from numerical simulation, based on the theory, of the AUT. The reconstruction algorithm compensates for the missing information with a-priori knowledge of the antenna under test (e.g. the antenna geometry) to reach a proper hybridization of measurements and simulations.

The work will be organized as follow. In chapter 1 there will be a brief introduction to antenna background and simulations. Then in chapter 2 it will be introduced the theory behind the NF and FF reconstruction process based on the work reported in [1]. In chapter 3 and chapter 4 it will be presented the reconstruction process applied to two different cases: a 2x1 strip dipole array and a 4x1 patch array. The dipole reconstruction represents a very ideal case which will be functioning as a test run for the code. In this part of the work there will not be dedicated much attention to the robustness of the methods themselves nor to the reduction of measurement points used (i.e. trying to reconstruct the full array FF with the minimum number of sampled points for the single element dimension), instead, it will function as a verification of the feasibility of the reconstruction process. The main purpose of this thesis will be presented in chapter 4, where it will be simulated a linear array patch antenna with 4 elements and exploited different setups for the measurement and try to reduce the sampled data as much as possible while observing the obtained results.

Acknowledgements

I would like to express my gratitude to my supervisor, Marco Righero, who guided me throughout this project and my professor Giuseppe Vecchi. I would also like to thank my family and my friends who supported me. I wish to extend my special thanks to SEDS Italy who gave me lots of opportunities.

Contents

List of Tables	6
List of Figures	7
1 Introduction	11
1.1 Antenna background	12
1.1.1 Field Regions	13
1.1.2 Radiation pattern	14
1.1.3 Measurement properties of antennas	16
1.2 Microstrip Antennas	17
1.2.1 Array Antennas	17
1.2.2 Far-Field Approximation	19
1.3 Antenna simulations	20
1.4 Simulation Accuracy	23
2 Inverse Equivalent Surface-Source Problem	25
2.1 General Equivalence Problem	25
2.2 Method of Moments	27
2.3 Basis functions	28
2.3.1 RWG basis functions	28
2.4 IESSS : Inverse equivalent surface-source solution	29
3 Dipole reconstruction	33
3.1 Dipole array reconstruction	39
3.2 Auxiliary sources	42
3.2.1 NF difference	42
3.2.2 Auxiliary sources	44
3.3 FF reconstruction methods comparison	48
4 Antenna Array Reconstruction	51
4.1 Antenna design	51
4.1.1 Subsampling	53
4.2 Reconstruction with 28 points	54
4.2.1 Linear array reconstruction	56
4.2.2 Auxiliary sources	60
4.3 Reconstruction with 190 points	65

4.3.1	Reconstruction with only auxiliary sources	68
5	Conclusion	71
5.0.1	Research limitations	73
A		75
A.1	Surface Equivalence Principle Review	76
A.2	The Least Square Method	77
A.3	Time domain solver overview	77
	Bibliography	79

List of Tables

1.1	Post-processing toolbox parameters	20
1.2	Approximation error between spherical coordinate components and cartesian components represented in spherical coordinates.	23
3.1	Comparison between different distribution of auxiliary sources for the FF reconstruction of the linear array.	47
3.2	Comparison between different distribution of auxiliary sources for the FF reconstruction of the linear array.	50
4.1	Antenna design parameters.	51
4.2	Minimum number of sampling points from theoretical formula and the actual sampling points exported form CST.	53
4.3	List of acronyms used in the reconstruction equations.	60
4.4	Auxiliary sources and their relative FF reconstruction error.	61
4.5	Reconstruction errors results at 28 sampled points of all three reconstruction methods.	65
4.6	Reconstruction errors results between 28 and 190 sampled points.	68

List of Figures

1.1	Representation of the radiated field in spherical coordinates system.	12
1.2	Fields regions.	14
1.3	Two-dimensional normalized field pattern.	15
1.4	Two dimensional plot of normalized field pattern in dB	16
1.5	Geometrical representation of a microstrip patch rectangular antenna.	17
1.6	The Eurofighter Typhoon combat aircraft with its nose fairing removed, revealing its Euroradar CAPTOR AESA radar antenna. Active Electronically Scanned Array (AESA) is a computer-controlled phased antenna array, which means that the beam of radio waves can be steered to different directions. (source: Wikipedia)	18
1.7	Fujikura 28 GHz PAAM (Phased Antenna Array Module) for 5G millimeters wave (mmWave) applications. (source: Fujikura website)	18
1.8	Beam Forming Network representation with each individual exiting currents for each element of the array.	19
1.9	Field export in arbitrary coordinates from CST Studio. 2D Field evaluation toolbox (left), observation points on a sphere around the AUT (right).	21
1.10	Field export in arbitrary coordinates from CST: 1953 observation points.	21
1.11	Exported E-field Theta component, E_θ , represented in NF in MATLAB (left) and compared to CST 3D plot in FF (right)	22
1.12	Exported E-field Phi component, E_ϕ , represented in NF in MATLAB (left) and compared to CST 3D plot in FF (right)	22
2.1	Illustration of the Equivalence Theorem, original (left) and general (right).	26
2.2	RWG basis function representation.	28
2.3	Rectangular surface represented with RWG basis functions.	29
2.4	Closed surface around the AUT, r' ; source locations, r : observation locations.	30
3.1	Reconstruction surface Σ_R of a single dipole.	33
3.2	Sampled points on a sphere at the observation distance of 5λ around the AUT.	34
3.3	Surface density equivalent currents reconstructed on Σ_R	35
3.4	NF reference (left) and NF reconstructed (right) represented as intensity points (in dB) on a sphere with radius equal to the distance if the observation locations.	36
3.5	NF reference (left) and NF reconstructed (right) cuts at $\phi = 90^\circ$	36
3.6	FF radiation pattern, reference (left) and reconstructed (right).	37
3.7	FF pattern cut at $\phi = 0^\circ$, reference (blue) and reconstructed (red).	38

3.8	FF pattern cut at $\phi = 90^\circ$, reference (left) and reconstructed (right). . . .	38
3.9	Strip dipole array model from CST simulation (left) and reconstruction surface (right).	39
3.10	Reconstruction surfaces shifted for each element of the strip dipole array. .	39
3.11	Electric field intensity for each element of the linear array.	40
3.12	Electric field intensity of the linear array, reference NF (left) and reconstructed NF (right).	41
3.13	Electric field pattern of the linear array at $\phi = 90^\circ$, reference NF (blue) and reconstructed NF (red).	41
3.14	Electric field difference with the reference.	42
3.15	J (electric) and M (magnetic) current hotspots represented as colored points on the reconstruction surface for the entire dipole array.	43
3.16	Sum between the electric field difference with the reconstructed electric field, at NF, to confirm the reconstruction error.	43
3.17	Representation of a singular auxiliary source constituted by 11 RWG basis functions, l is the sources dimension and is equal to $\lambda/5$	44
3.18	Representation of a distribution of auxiliary sources (red) around the array. $N_{AUX} = 24$	45
3.19	E-field reconstruction with 24 auxiliary sources at $5 \cdot 10^{-4}$ tolerance.	45
3.20	E-field reconstruction with 24 auxiliary sources at 10^{-6} tolerance.	45
3.21	Representation of a distribution of auxiliary sources (red) around the array. $N_{AUX} = 54$	46
3.22	E-field reconstruction with 54 auxiliary sources for a given tolerance of 10^{-6}	46
3.23	Representation of a distribution of auxiliary sources (red) around the array. $N_{AUX} = 96$	47
3.24	E-field reconstruction with 96 auxiliary sources for a given tolerance of 10^{-6}	47
3.25	Direct inverse-source reconstruction of the entire array, reconstruction surface (left) and FF cut at $\phi = 90^\circ$ (right).	48
3.26	Reconstruction only by translating the reconstruction surface, Σ_{R1}, Σ_{R2} (left), and FF reconstructed at $\phi = 90^\circ$ (right).	49
3.27	Reconstruction with auxiliary sources. Sources distribution (left) and FF cut at $\phi = 90^\circ$ (right).	49
4.1	Single patch antenna structure (left) and electric field radiation pattern in far field (right).	52
4.2	Linear array antenna structure (left) and electric field radiation pattern in far field (right).	52
4.3	Minimum sphere around the AUT.	53
4.4	Sampled point around the microstrip patch antenna, at distance 5λ , reported in MATLAB. 28 points (left), 190 points (right).	54
4.5	Single patch reconstruction surface (Σ_R), δ is the gap, in red the actual dimension of the metal patch, and in blue the dimension of the substrate.	54
4.6	Representation at the two main cut $\phi = 0^\circ, \phi = 90^\circ$	55
4.7	Representation at the two main cut $\phi = 0^\circ, \phi = 90^\circ$	56
4.8	Linear array reconstruction surface (Σ_R).	56

4.9	Representation of each single element reconstruction surface and their relative reconstructed surface currents (J_{eq}^{LOVE} , M_{eq}^{LOVE}), and the reconstructed near fields $E_{NF,RECn}$, with n as the number of element in the array.	57
4.10	E-field NF reconstruction only by translation, of the linear array, cuts at $\phi = 0^\circ$ and $\phi = 90^\circ$	58
4.11	E-field FF reconstruction only by translation, of the linear array, cuts at $\phi = 0^\circ$ and $\phi = 90^\circ$	58
4.12	E-field NF difference of the linear array, cuts at $\phi = 0^\circ$ and $\phi = 90^\circ$	60
4.13	E-field NF sum, cuts at $\phi = 0^\circ$ and $\phi = 90^\circ$	61
4.14	Distribution of 24 auxiliary sources around the linear array (left), FF pattern reconstructed (right).	62
4.15	Distribution of 42 auxiliary sources around the linear array (left), FF pattern reconstructed (right).	62
4.16	Distribution of 64 auxiliary sources around the linear array (left), FF pattern reconstructed (right).	63
4.17	E-field NF reconstructed versus the reference E-field of the linear array for all the previous auxiliary source configurations.	63
4.18	FF reconstructed normalized in directivity for each auxiliary source configurations with their relative reconstruction error.	64
4.19	FF reconstruction with inverse-source of the linear array using 28 sampled points.	64
4.20	FF reconstruction of the linear array considering only the information from the auxiliary sources.	65
4.21	NF reconstructed (red) and NF reference (blue) of the single patch using 190 sampled points.	66
4.22	FF reconstructed (red) and FF reference (blue) of the single patch using 190 sampled points.	66
4.23	FF reconstruction normalize in directivity from applying the inverse-source to all the array structure.	67
4.24	FF reconstruction normalize in directivity from translation of the reconstruction surface in each array element position, using the coefficients evaluated from the single element.	67
4.25	FF reconstruction normalize in directivity using the translating element and auxiliary sources.	68
4.26	FF reconstruction normalize in directivity using only auxiliary sources (28 sampled points).	69
5.1	FF reconstruction normalize in directivity for 28, 32 and 98 sampled points with their relative reconstruction error, using 16 auxiliary sources.	72
5.2	FF reconstruction normalize in directivity for 28, 32 and 98 sampled points with their relative reconstruction error, using 42 auxiliary sources.	72
5.3	FF reconstruction normalize in directivity comparing the standard method with the new one proposed in this thesis.	73
A.1	Surface equivalence principle representation.	76

"In so far as a scientific statement speaks about reality, it must be falsifiable: and in so far as it is not falsifiable, it does not speak about reality."

[KARL R. POPPER, *The Logic of Scientific Discovery*]

Chapter 1

Introduction

Fast antenna measurement has been very popular in the last decade. New progress in communication systems requires more complex antenna designs that imply increasing manufacturing and testing stages during which many sources of error can affect the antenna's final prototype, degrading its overall performance and then it requires new design steps to detect and fix these manufacturing errors. This work of thesis aims to reduce the number of sampling points needed for antenna testing below the Nyquist limit by integrating the missing information from numerical simulation, based on the theory, of the AUT.

The antenna near the field is defined as the field in the proximity of the AUT (i.e. with a distance $< \lambda^1$) and is strongly related to the physical currents of the radiating object. So an accurate measure of the near field provides an advantageous mapping of the far field and currents distribution on the antenna.

The work will be organized as follow. In the next section, after a brief introduction to antenna background, it will be introduced the theory behind the NF and FF reconstruction process based on the work reported in [1]. Then Chapter 1 and Chapter 2, it will present the reconstruction process applied to two different cases: a 2 x 1 strip dipole array and a 4 x 1 patch array. The dipole reconstruction represents a very ideal case which will be functioning as a test run for the code. In this part of the work, there will not be dedicated much attention to the robustness of the methods themselves nor to the reduction of measurement points used (i.e. trying to reconstruct the full array FF with the minimum number of sampled points for the single element dimension), instead, it will function as a verification of the feasibility of the reconstruction process. Then, as a second part of the work, it will be simulated a linear array patch antenna with 4 elements and exploited different setups for the measurement and try to reduce the sampled data as much as possible while observing the obtained results.

Finally, the main purpose of this thesis will be presented in chapter 4 where the reconstruction of the electric field of a real antenna will be compared to the simulation results to check the validity of this method.

¹ λ represent the *wavelength* which is defined as the ratio of the speed of light in vacuum over the frequency, $\lambda = \frac{c_0}{f}$

To compare the success and validity of the reconstruction, it was compared the intensity of the electric field on a sphere around the AUT and also the plots of its main cuts: fixing on the spherical coordinates system in Figure 1.1 the angle $\phi = 0^\circ$ and $\phi = 90^\circ$, the resulting two dimensional plots are in function of θ . The plot results are always represented with the reference field exported from CST Studio simulations.

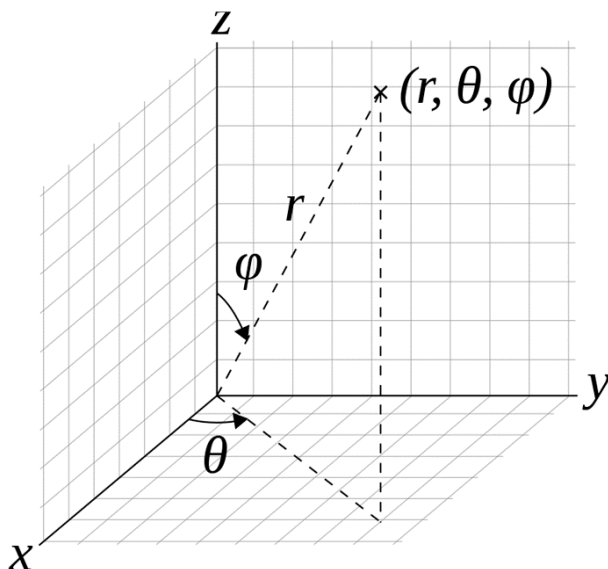


Figure 1.1. Representation of the radiated field in spherical coordinates system.

The main parameter is the reconstruction error which indicates the relative difference between the reconstructed field versus the reference one.

1.1 Antenna background

Before introducing the theory an overview of antennas and their characteristic parameters has to be done. The IEEE Standard Definitions of Terms for Antennas (IEEE Std 145-1983) defines the antenna as "*a means for radiating or receiving radio waves*".

Antennas are a key component in wireless communications systems which provide the necessary coupling between circuit and open space allowing the transfer of information between a TX² and an RX³ via free-space radiation propagation. The TX antenna is the element that is fed by a power source and transforms the electromagnetic field into free-space electromagnetic waves. The RX antenna, instead, transform the incident wave into power along the transmission line linked to the receiver system.

²The acronym TX stands for Transmitting

³The acronym RX stands for Receiving

The radiation intensity is defined as the power which is radiated per unit solid angle ⁴. In the far field zone the radiation can be expressed as:

$$U(\theta, \phi) = \frac{r^2}{2\eta} |E(r, \theta, \phi)|^2 \quad (1.1)$$

where $E(r, \theta, \phi)$ is the electric field in spherical coordinates, $\eta = Z = \text{sqrt}(\eta_0\eta_r)/(\epsilon_0\epsilon_r)$ is the medium characteristic impedance and r is the distance.

Directivity

The antenna directivity is defined as the ratio between the antenna radiation intensity, U , and the isotropic radiation intensity, U_0 , in a given direction.

$$D = \frac{U}{U_0} = \frac{4\pi U}{P_{rad}}, \quad U_0 = \frac{P_{rad}}{4\pi} \quad (1.2)$$

Gain

The antenna gain is defined as the ratio between the field radiation intensity and the isotropic radiation intensity. (source: Antenna Theory: Analysis and Design: A. Balanis [2])

$$G = 4\pi \frac{U(\theta, \phi)}{P_{rad}} \quad (1.3)$$

1.1.1 Field Regions

The radiating space surrounding an antenna is divided into two main regions: Near-Field and Far-Field. The radiating Near-Field region (*Fresnel*) is defined as the sphere with radius $R_2 = 2D^2/\lambda$, where D is the largest dimension of the AUT and λ the wavelength. Instead, the closest space surrounding the antenna is called the reactive Near-Field region defined inside the sphere with radius $R_1 = 0.62\sqrt{D^3/\lambda}$.

⁴In geometry a solid angle is the measure of the amount of the field of view (i.e. the amount of the observable world that can be seen at a precise moment) from a particular point of view of a given object. (source: Wikipedia)

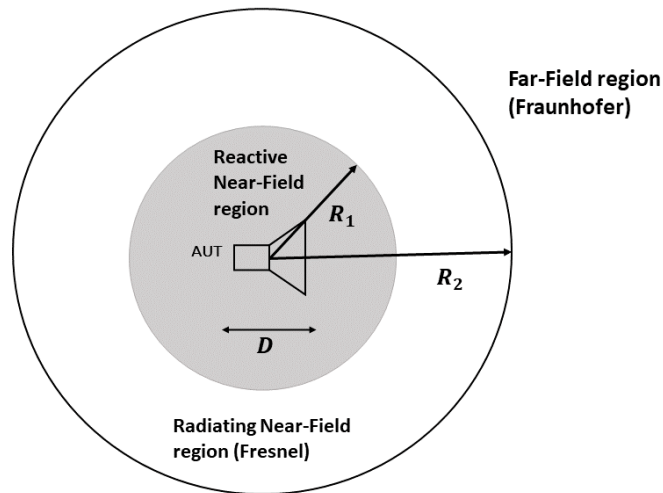


Figure 1.2. Fields regions.

The Far-Field region (*Fraunhofer*) is defined as the region where the field distribution of the antenna is independent of the distance from the antenna, which exists from a distance greater than $2D^2/\lambda$. When the distance $|R|$ is small (i.e. a few wavelengths) the coupling aspect is affected by the instantaneous distribution of charge over the antenna surface. As the distance increases the radiated power is no longer dominated by these effects. That is the way the antenna radiation pattern characterization takes place in far-field.

1.1.2 Radiation pattern

The radiation pattern of an antenna is defined as "a mathematical function or a graphical representation of the radiation properties of the antenna as a function of space coordinates.." [2]. The antenna radiation pattern is graphically represented in Figure 1.3 as a function of spherical coordinates.

The antenna pattern is usually been analyzed by looking at its electric and magnetic field planes (E-field, H-field), where the E- and H- field lie one, respectively. These planes are orthogonal to each other because the two fields are orthogonal to each other as well.

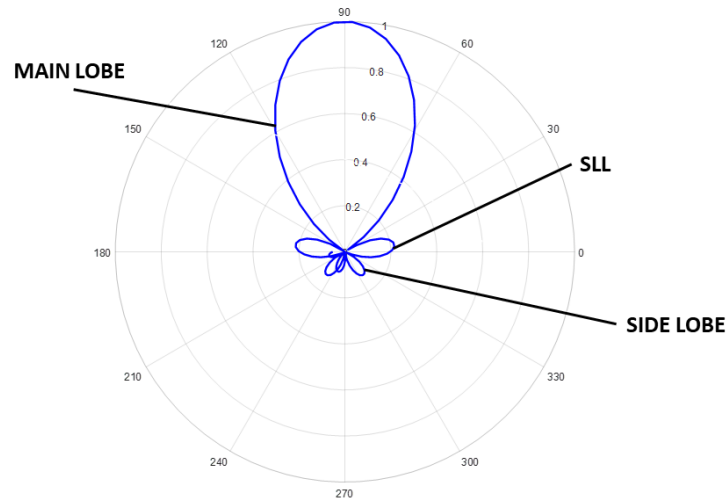


Figure 1.3. Two-dimensional normalized field pattern.

Antenna's radiation pattern can be subdivided in regions that present local maximum separated by points where the radiation drop to zero, called *nulls*. These radiation portions are called *lobes* and they can be classified as follows:

- **MAIN LOBE:** is the radiation major lobe containing the direction of the maximum radiation.
- **SIDE LOBE:** is a lobe that points in any direction other than the main one.
- **SLL:** *Secondary Lobes Level* is defined as the value of the side lobe adjacent to the main beam.

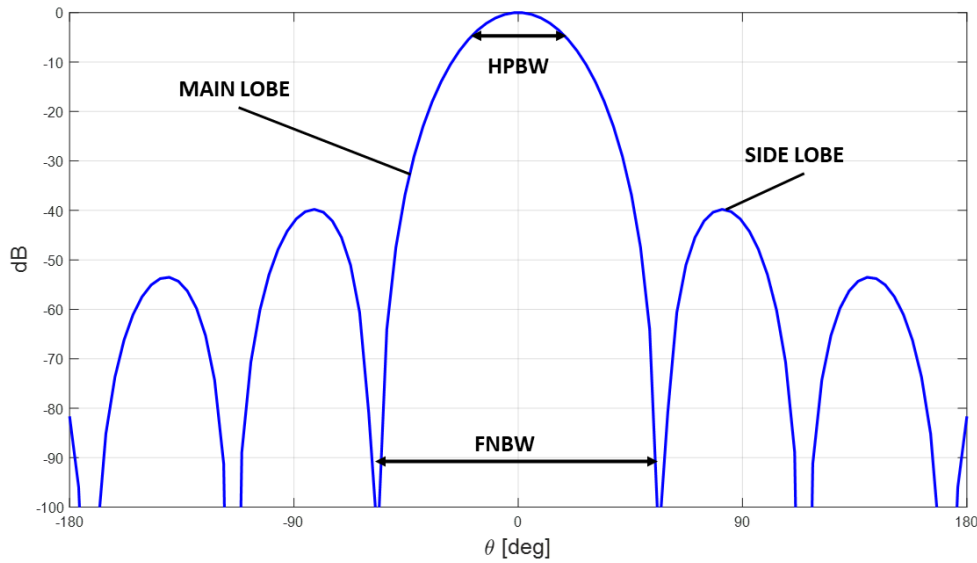


Figure 1.4. Two dimensional plot of normalized field pattern in **dB**.

Another important parameter related to the radiation pattern of an antenna is the *beamwidth* that represents the angular distance between two identical points at the opposite side of the main lobe.

- **HPBW**: the angular separation in which the radiation pattern decreases by -3dB from the peak of the main lobe.
- **FNBW**: the angular span between the first pattern nulls adjacent to the main lobe.

1.1.3 Measurement properties of antennas

Antennas can be described by their mass and physical size. When they are connected with an active electric circuit, antennas manifest electrical properties, then they became able to radiate or receive radio waves. The main measurable characteristic of an antenna is its ability to radiate power in a given direction. Antennas do not radiate equally in every direction, therefore the variation in the ratio of radiated power is the parameter to be measured. Using a spherical coordinate system where the antenna is placed at the centre, its radiation pattern, both electric and magnetic field, can be characterized as a function of the angle θ and ϕ .

Antenna measurements

The antenna test range objective is to characterize an antenna in a known configuration to the extent to which its coupling can be predicted in other situations.

1.2 Microstrip Antennas

Microstrip antennas have been very popular in the 1970s for space applications and today are used also in commercial fields. These types of antennas consist of a metallic patch on a grounded substrate. The patch can take different shapes but the rectangular and circular ones are the most used due to their simple fabrication and analysis process, and also their attractive radiation characteristics. Microstrip antennas are compatible with PCB⁵ design and MMIC⁶ design. They are very versatile in terms of resonant frequency, pattern polarization and impedance. These types of antennas can be found on the surface of high-performance aircraft, satellites, missiles, cars and smartphones.

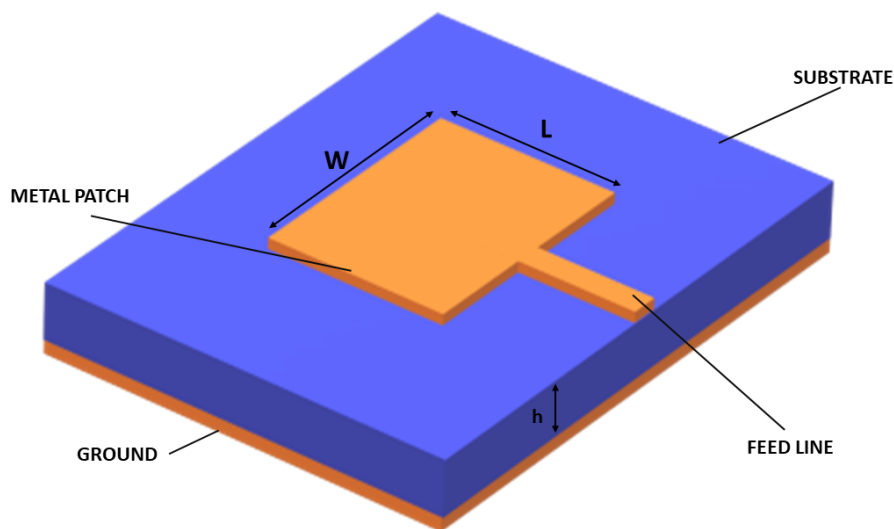


Figure 1.5. Geometrical representation of a microstrip patch rectangular antenna.

1.2.1 Array Antennas

By applying a set of patch antennas it is possible to achieve better radiation characteristics for many applications. Array antennas are geometrical aggregation of radiating elements such that the radiation from the elements adds up to give a maximum radiation intensity in a specific direction.

⁵PCB stands for Printed Circuit Board, it is a laminated sandwich structure of conductive and insulating layers.

⁶MMIC stands for Monolithic Microwave Integrated Circuit which is a type of integrated circuit (IC) device that operates at microwave frequencies (300 MHz to 300 GHz).



Figure 1.6. The Eurofighter Typhoon combat aircraft with its nose fairing removed, revealing its Euroradar CAPTOR AESA radar antenna. Active Electronically Scanned Array (AESA) is a computer-controlled phased antenna array, which means that the beam of radio waves can be steered to different directions. (source: Wikipedia)

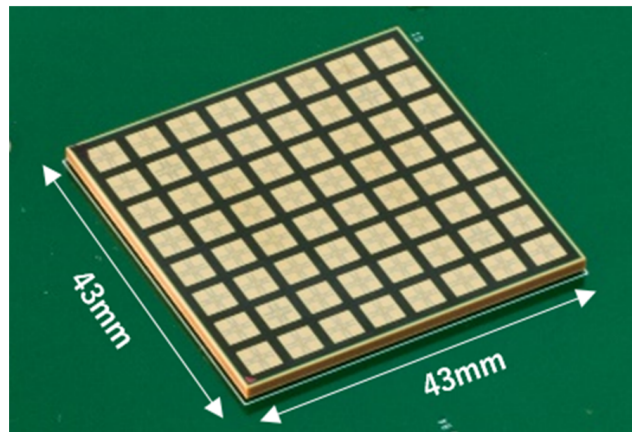


Figure 1.7. Fujikura 28 GHz PAAM (Phased Antenna Array Module) for 5G millimeters wave (mmWave) applications. (source: Fujikura website)

Array antennas are constituted by a feeding network (Beam Forming Network BFN) and a set of radiating parts, which in the case discussed in this thesis it is a 4 square patch antennas. The reconstruction process involves only the electric field of the AUT. The radiation pattern of the array when all its parts are fed is a linear combination of the single patterns of each patch antenna.

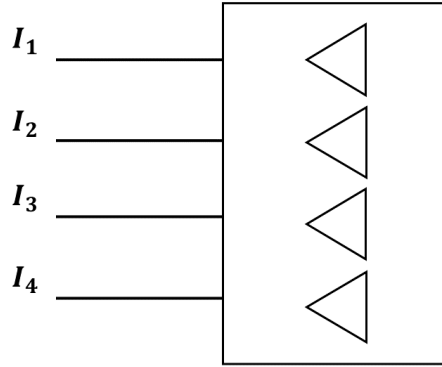


Figure 1.8. Beam Forming Network representation with each individual exiting currents for each element of the array.

Electric field of the total array:

$$\underline{E}_n(r, \theta, \phi) = \sum_n I_n \underline{E}_n(r, \theta, \phi) \quad (1.4)$$

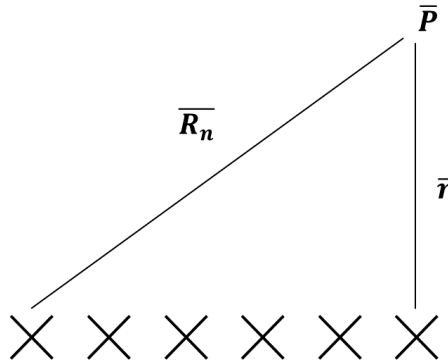
I_1, I_2, I_3, I_4 are the feeding currents from the BFN. Neglecting inter-element coupling:

$$\underline{E}_n(r, \theta, \phi) = \frac{-jZ_0}{2\lambda} 4\pi g(R_n) I_n \underline{h}_{e_n}(\hat{R}_n) g(R_n) = \frac{e^{-jkR_n}}{4\pi R_n} \quad (1.5)$$

$\underline{R}_n = R_n \hat{R}_n$ is the position of the observation points, \underline{h}_{e_n} the effective height of the n-th element.

1.2.2 Far-Field Approximation

At FF the distance between each radiating objects is much smaller than the distance at which the field is calculated, so the following approximation stands $|r_n| \ll r$.



$$g(R_n) = \frac{e^{-jkR_n}}{4\pi R_n} = \frac{1}{R_n} \frac{e^{-jkR_n}}{4\pi} \quad (1.6)$$

Then follow the approximation $\frac{1}{R_n} \approx \frac{1}{r}$.

$$g(R_n) = \frac{e^{-jkR_n}}{4\pi R_n} = \frac{e^{-jkr}}{4\pi r} \exp(jk\hat{r} \cdot \underline{r}_n) \quad (1.7)$$

Then for identical equi-oriented and equi-polarized radiating elements:

$$\underline{E}(r, \theta, \phi) \approx -j \frac{Z_0 4\pi}{2\lambda} \frac{e^{-jkr}}{4\pi r} h_e(\theta, \phi) \sum_n I_n \exp(jk\hat{r} \cdot \underline{r}_n) \quad (1.8)$$

For the design of an antenna array starting from the single element, it is important to choose an appropriate inter-element distance d which characterizes the **gain** and **directivity** of the full antenna structure. Also the larger the number of elements, the more complex the BFN.

1.3 Antenna simulations

To have the best characterization of the AUT, both the single element on which there are calculated the surface current density coefficients and the linear array, it was used a high-performance 3D EM analysis software, CST Studio Suite. The simulations of the radiating objects were used for extrapolating the E-field at NF and FF to MATLAB.

Numerical simulations need to be compared with real data. To have a realistic reference of the problem, the data obtained from the simulation software CST was put in comparison with the same data exported in MATLAB. The electric field components, in spherical and cartesian coordinates, have been re-computed and evaluated. The single patch antenna has been synthesized by using CST and simulating its electric field inside a finite region of space of $20\lambda \times 20\lambda$. The post-processing toolbox allows exporting field values in arbitrary positions in space, by choosing a coordinate system. The exported field has been evaluated at 5λ , 10λ and 20λ .

coordinate system	spherical
normal	R
stepsize	λ
sphere radius	5λ
theta	-180:180
phi	-90:90

Table 1.1. Post-processing toolbox parameters

Defining the parameters in Table 1.1 the post-processing toolbox creates a sphere of samples with arbitrary radius and stepsize, Figure 1.9.

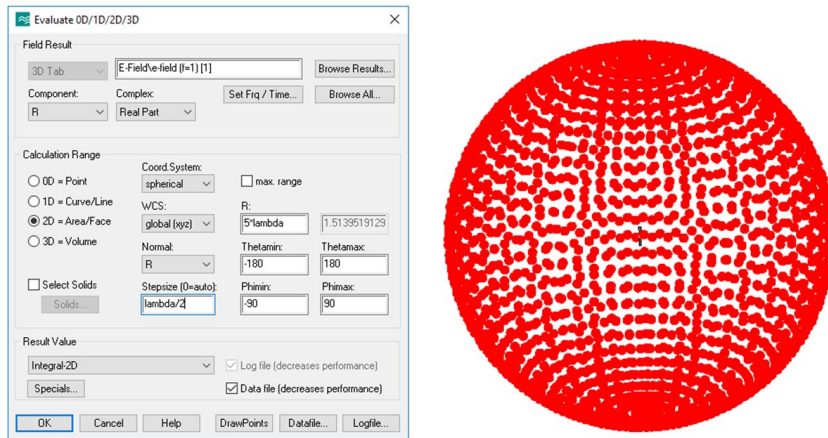


Figure 1.9. Field export in arbitrary coordinates from CST Studio. 2D Field evaluation toolbox (left), observation points on a sphere around the AUT (right).

For each component of the E-field, R , Θ and Φ it was exported separately their real and imaginary parts, plus a .xyz file containing the selected observation points, displayed as red dots in Figure 1.10.

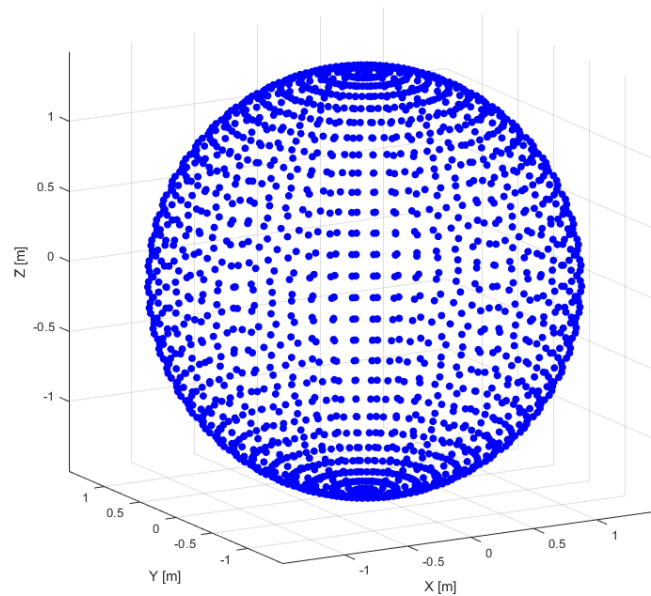


Figure 1.10. Field export in arbitrary coordinates from CST: 1953 observation points.

Here is reported a comparison between the exported E-field in 2450 arbitrary points on a sphere around the AUT, with a radius equal to 5λ , from the CST simulation, with the same radiated field but evaluated at far-field directly from the CST 3D plot. This representation was used to verify that the data used for the reconstruction of the dipole currents and field was reliable, at least shape-wise because the field values are not exactly the same in FF and NF.

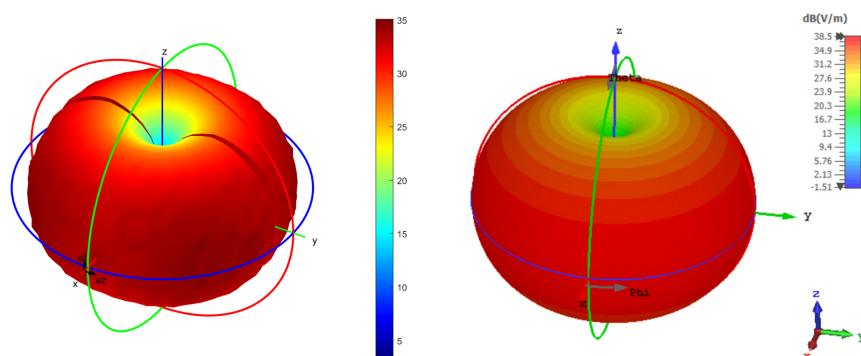


Figure 1.11. Exported E-field Theta component, E_θ , represented in NF in MATLAB (left) and compared to CST 3D plot in FF (right)

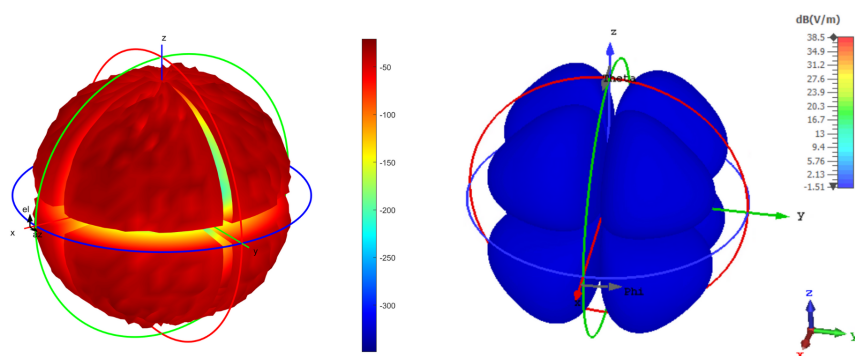


Figure 1.12. Exported E-field Phi component, E_ϕ , represented in NF in MATLAB (left) and compared to CST 3D plot in FF (right)

In Table 1.3 is reported the relative error of each field components between the exported

version in spherical coordinates and the one converted in cartesian coordinates.

ΔE_θ	1.809910^{-5}
ΔE_ϕ	1.812710^{-5}
ΔE_ρ	1.335110^{-4}

Table 1.2. Approximation error between spherical coordinate components and cartesian components represented in spherical coordinates.

1.4 Simulation Accuracy

It is also important to specify the limits of the simulation environments which will be the possible source of systematic errors. Starting from the structure of the patch antenna itself which is one of the most complex radiating objects to represent and analyze. To get accurate results from these simulations is important to choose the correct mesh parameters. CST provides different mesh, and geometry models:

- Hexaedral
- Tetrahedral

and a set of electromagnetic simulation solvers:

- Time Domain
- Frequency Domain
- Eigenmode

A fine **Hexaedral** mesh with a **Time Domain solver** was used to carry out all the simulation data used in this thesis. Another important aspect to take into account is the characterization of the radiated field of a patch antenna which is one of the more complex structures to analyze. The main aspect of this work is the reduction of the number of sampled points on a sphere around the AUT to calculate the antenna currents and its FF. Therefore the accuracy of the selected points plays a very important role in the reconstruction process. Unfortunately, it is not possible to manually select the best sampling points with the Post-processing toolbox in CST. So the choice was entirely given to the software and this could also have been a source of error in the reconstruction process of the entire array.

Chapter 2

Inverse Equivalent Surface-Source Problem

The inverse equivalent surface-source (IESS) formulation is depicted in Figure 2.1. The reconstruction process presented in this thesis, for the NF of the simulated antenna, is based on the work from [1], which proposes a solution of the IESSP (Inverse Equivalent Surface-Source Problem) with different forms of side constraints such as the Love condition. The source reconstruction problem aims to obtain currents with a known location that radiate vector field information.

The solution adopted in this work is based on a reconstruction via equivalence currents on a closed surface around the radiating object. The currents are obtained by applying the **inverse-source** method with Love's constraint. The NF-to-FF transformation then is exploited to represent the resulting E-field in FF. The problem is formulated in terms of linear integral equations and has been addressed by several works in the past years. In [3] is reported a unified framework of the various possible formulations of the source reconstruction problem.

2.1 General Equivalence Problem

Here is summarized the general equivalence problem discussed in [3]. The problem described in Figure 2.1 aims to find sources on the closed reconstruction surface, denoted by Σ_R , that radiate the input electric field tangent to the measurement surface denoted by Σ_M . Defining \vec{E}'_-, \vec{H}'_- as the fields inside the reconstruction surface Σ_R , and \vec{E}'_+, \vec{H}'_+ as the fields outside Σ_R , the equivalence currents on the closed surface can be expressed as:

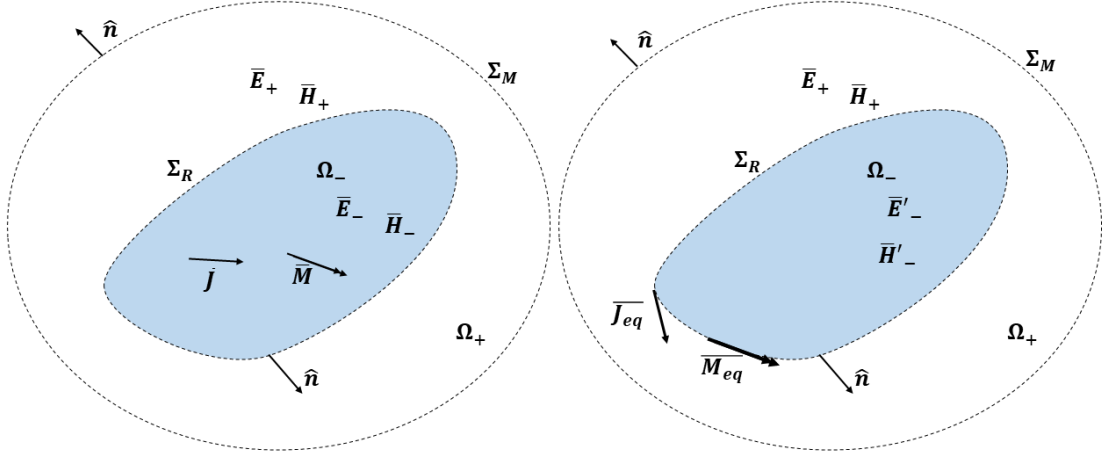


Figure 2.1. Illustration of the Equivalence Theorem, original (left) and general (right).

$$\begin{cases} J_{eq} = \hat{n} \times [H_+(r) - H'_-(r)] \\ M_{eq} = -\hat{n} \times [E_+(r) - E'_-(r)] \end{cases}, \quad r \in \Sigma_R \quad (2.1)$$

By using the free-space radiation operator L , M which will be referred to as EJ and EM respectively in the reconstruction equations.

$$\begin{cases} L = \int \int \int_{V_w} \delta(r - r_m) \cdot \int \int_{\Sigma_R} \bar{G}_J^E(r, r') \cdot \frac{\beta(r')}{Z} da' dv \\ M = \int \int \int_{V_w} \delta(r - r_m) \cdot \int \int_{\Sigma_R} \bar{G}_M^E(r, r') \cdot \beta(r') da' dv \end{cases} \quad (2.2)$$

With G the Gram matrix, defined as:

$$G = \int \int_{\Sigma_R} \beta_S(r) \cdot \beta_p(r') \quad da' da \quad (2.3)$$

Then it is possible to express the electric field as:

$$E(r) = -\eta_0 L(J_{eq}; r) + K(M_{eq}; r), \quad \eta_0 = \sqrt{\mu_0/\epsilon_0}, \quad k_0 = \omega \sqrt{\mu_0 \epsilon_0} \quad (2.4)$$

Love's constraint

The Love equivalence formulation takes the fields inside the reconstruction surface as null, and the surface currents are chosen to sustain the exterior fields \bar{E}'_+ , \bar{H}'_+ . If it is set the interior fields equal to zero, the result is Love's form of the Equivalence Principle.

$$\begin{cases} \hat{n} \times H_+(r) = J_{eq}^{LOVE} \\ -\hat{n} \times E_+(r) = M_{eq}^{LOVE} \end{cases}, \quad r \in \Sigma_R \quad (2.5)$$

With Love's equivalence, fields on the boundary are obtained directly from the equivalent currents, which is very important for antenna diagnostics because the resultant fields and currents distribution can be used as a comparison with the initial design of the AUT to identify the parts of the antenna that have faults or present discrepancies. Fields radiated by the currents on Σ_R in the region external to Σ_M are obtained by using Green's function of the free space.

$$\hat{n} \times E(r) = \hat{n} \times [-\eta_0 L(J_{eq}; r) + K(M_{eq}; r)], \quad r \in \Sigma_M \quad (2.6)$$

Computing Love's equivalent currents $J_{eq} = \hat{n} \times H$ and $J_{eq} = -\hat{n} \times E$ on σ_R that radiate the same fields inside σ_R as the original one. Then, to obtain the actual fields on the reconstruction surface Σ_R directly from the current in 2.5, the zero fields of Love's equation must be enforced.

$$\hat{n} \times E_-(r) = \lim_{r \rightarrow \Sigma_R^-} \hat{n} \times [\eta_0 L(J_{eq}^{LOVE}; r) + K(M_{eq}^{LOVE}; r)] = 0 \quad (2.7a)$$

$$\hat{n} \times H_-(r) = \lim_{r \rightarrow \Sigma_R^-} \hat{n} \times \left[-\frac{1}{\eta_0} L(M_{eq}^{LOVE}; r) - K(J_{eq}^{LOVE}; r) \right] = 0 \quad (2.7b)$$

2.2 Method of Moments

The Method of Moments is a numerical method in computational electromagnetics. It is a frequency-domain-based method which involves the projection of an integral equation into a system of linear equations, by applying specific boundary conditions. It uses a discrete mesh and finite element methods to model a surface (e.g. the reconstruction surface Σ_R), with the linear combination of pre-defined basis functions. The coefficients of these functions are the unknowns which will be the focus of the reconstruction method presented in this thesis. Given a deterministic problem the idea is to reduce a functional equation into a matrix equation.

$$L(f) = g \quad (2.8)$$

L is the operator, f is the field (unknown) and g represent the source. The expansion of f in a series of functions in the domain of L :

$$f = \sum_n \alpha_n f_n, \quad f_n : \text{basis functions} \quad (2.9)$$

A finite summation of f_n gives an approximate solution:

$$\sum_n \alpha_n L(f_n) = g \quad (2.10)$$

Assuming the inner product $\langle f, g \rangle$ has been determined and a set of weighted functions (or testing functions) w_1, w_2, w_3, \dots in the domain of L then taking the inner product with each W_m :

$$f = \sum_n \alpha_n \langle w_m, Lf_n \rangle = \langle w_m, g \rangle \quad (2.11)$$

The choice of $w_n = f_n$ is known as Galerkin's method. The approach used in [3] uses the Point-Matching method which is equivalent to using Dirac delta functions as testing functions.

2.3 Basis functions

The solution proposed in [1] involves the EFIE (Electric Field Integral Equation) with the Method of Moments (M.o.M.) in order to resolve scattering problems on arbitrarily shaped surfaces. Therefore the surface representation is the first step toward the discretization of the transmission equation 2.13. In this thesis, it was used a rectangular-shaped reconstruction surface which contains the AUT. This surface, which it will be called Σ_R from this point forward, is constituted by a set of basis functions.

2.3.1 RWG basis functions

For the solution of the IESSP (Integral Equation Surface-Source Problem), it was used the low-order Rao Wilton-Glisson (RWG) basis function [4] represents the electric and magnetic surface current densities discretization.

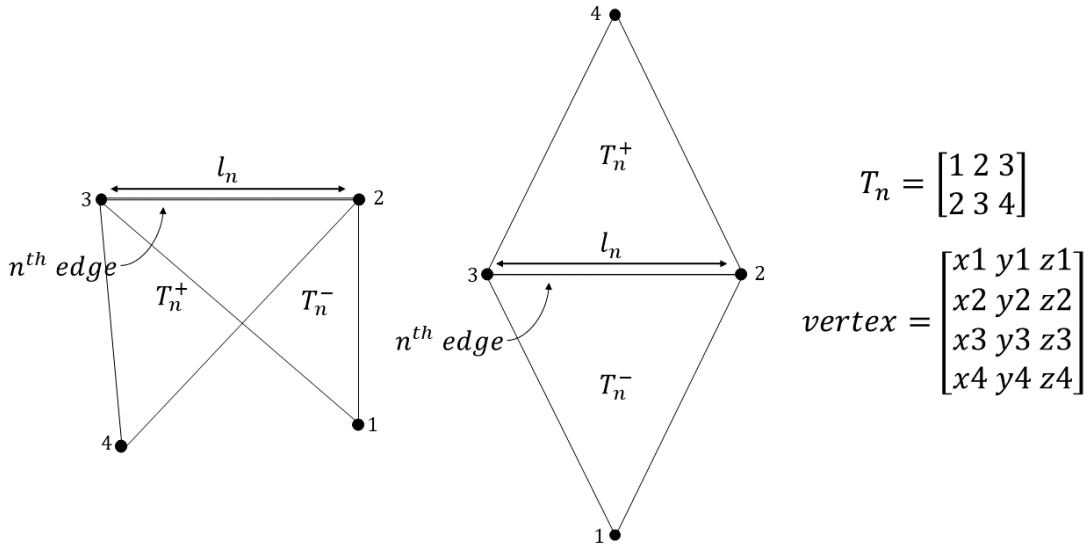


Figure 2.2. RWG basis function representation.

Each basis function is associated with a couple of cells T_n^+, T_n^- , defined by a set of three plus three vertices and an interior edge. It is defined by the following:

$$f_n(r) = \begin{cases} \frac{l_n}{2A_n^+} \rho_n^+, & r \in T_n^+ \\ \frac{l_n}{2A_n^-} \rho_n^-, & r \in T_n^- \\ 0, & \text{otherwise} \end{cases}, \quad r \in \Sigma_R \quad (2.12)$$

- l_n is the length of the edge.
- A_n is the area of the triangle.
- ρ_n is the position vector.

The basis function f_n was used to approximate the surface currents in 2.15.

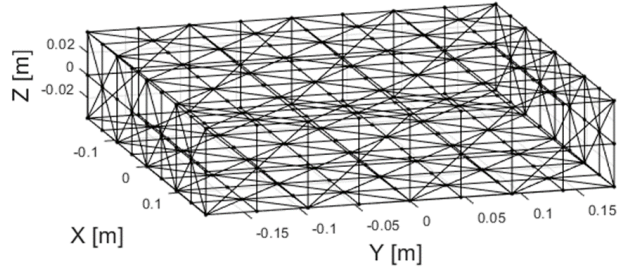


Figure 2.3. Rectangular surface represented with RWG basis functions.

2.4 IESSS : Inverse equivalent surface-source solution

In this section, it will be explained briefly the theory behind the code that performs the IESSP (Inverse Equivalent Surface-Source Problem) developed on [1]. J_{Σ_R} and M_{Σ_R} are the equivalent electric and magnetic surface densities on a closed surface Σ_R around the antenna under test (AUT) which contains all the radiation sources. The equivalent current densities J_{Σ_R} and M_{Σ_R} are the unknown quantities which should be determined.

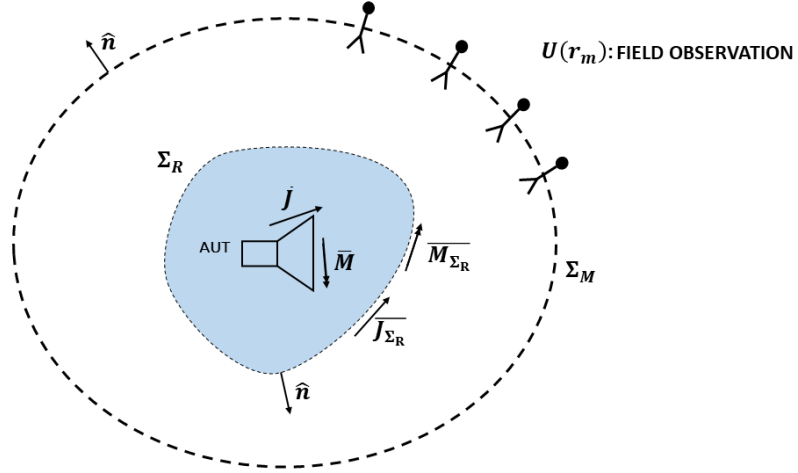


Figure 2.4. Closed surface around the AUT, r' ; source locations, r : observation locations.

Transmission equation:

$$U(r_m) = \int \int \int_{V_\omega} \delta(r - r_m) \cdot \int \int_{\Sigma_R} [\overline{G}_J^E(r, r') \cdot J_{\Sigma_R}(r') + \overline{G}_M^E(r, r') \cdot M_{\Sigma_R}(r')] da' dv \quad (2.13)$$

Σ_R is discretized via standar Method of Moments (M.o.M.) by projection into vector Dirac-delta functions which are the actual position and direction of the field samples on Σ_M (Point Matching). Imposing the Love condition for all observation points, it results that the surface current densities can be found by resolving these new equivalences:

$$J_{\Sigma_R}^{LOVE}(r') = \hat{n} \times H(r') \quad (2.14a)$$

$$M_{\Sigma_R}^{LOVE}(r') = -\hat{n} \times E(r') \quad (2.14b)$$

Discretization of electric and magnetic surface current densities by low-order RWG basis function β .

$$J_{\Sigma_R}^{LOVE}(r') = \sum_p J_p \beta_p(r') \quad (2.15a)$$

$$M_{\Sigma_R}^{LOVE}(r') = \sum_q M_q \beta_q(r') \quad (2.15b)$$

Eventually the IESSP can be expressed like the following:

$$\begin{bmatrix} EJ^\theta & EM^\theta \\ EJ^\phi & EM^\phi \end{bmatrix} \begin{bmatrix} J \\ M \end{bmatrix} = [U_m] = \begin{bmatrix} E_{NF,REF}^\theta \\ E_{NF,REF}^\phi \end{bmatrix} \quad (2.16)$$

EJ and EM are the free-space radiation matrices calculated on the observed points r'_m and from now on they will be referred to as:

$$EJ = \begin{bmatrix} EJ^\theta \\ EJ^\phi \end{bmatrix}, EM = \begin{bmatrix} EM^\theta \\ EM^\phi \end{bmatrix} \quad (2.17)$$

The inverse equivalent surface-source problem has more unknown coefficients than equations, it is then solved by applying the least mean square elements that give the surface current density coefficients J and M .

Chapter 3

Dipole reconstruction

This chapter introduces the reconstruction process through a simplified case of a linear array made of two dipoles. As specified in the introduction there will be no sampling points reduction. The main objective is to verify the correctness and applicability of the method proposed in Chapter 2. The single strip dipole is represented in Figure 3.1, and the resulting simulation data was exported as explained before with 1953 sampled points on a sphere with radius $5\lambda = 1.499$ m.

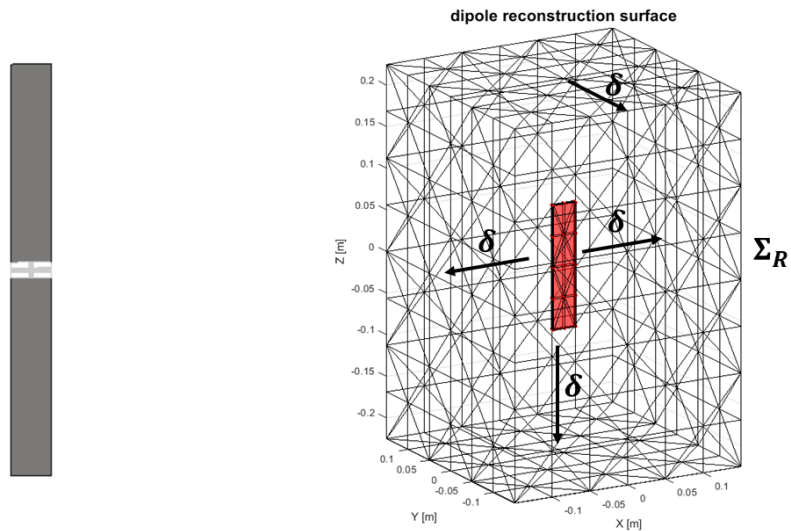


Figure 3.1. Reconstruction surface Σ_R of a single dipole.

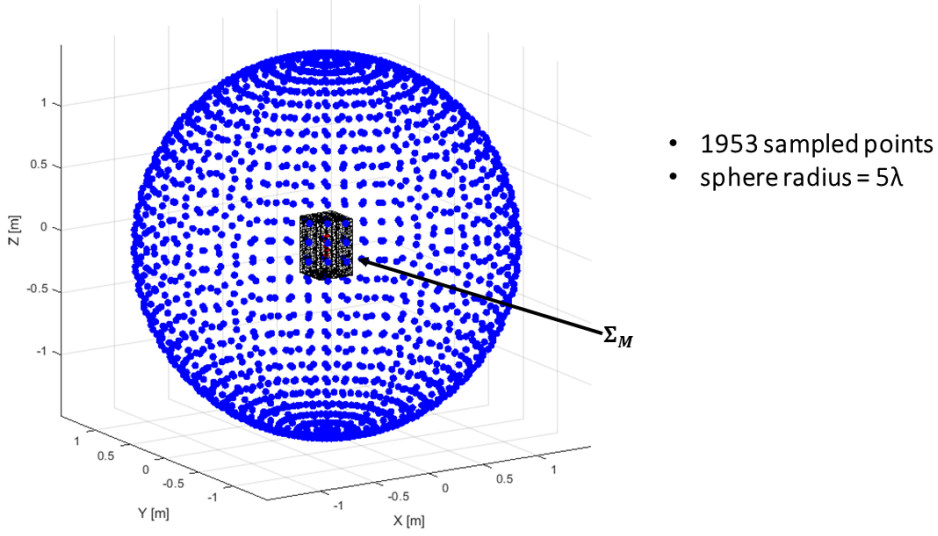


Figure 3.2. Sampled points on a sphere at the observation distance of 5λ around the AUT.

Now the geometry of the reconstruction problem has been defined. The same parameters for Σ_R will be used for each element of the array:

- $\delta = \lambda_0/2$
- mesh density = $\lambda_0/5$

Several simulations of the same radiating object with different mesh densities (which will be not reported here) have demonstrated that a value of $\lambda_0/5$ is enough to represent the field at FF. Finer density values were not necessary and it will only result in an increasing computation cost. The same thing is valid for the distance δ , which represents the gap between the actual dimensions of the AUT and the reconstruction surface around it. As explained in chapter 2, by resolving the discrete Love-constraint equation in a least-square sense, it is possible to compute the coefficients J_{eq}^{LOVE} , M_{eq}^{LOVE} to calculate the equivalent surface currents on Σ_R (Figure 3.3).

$$[EJ \quad EM] \begin{bmatrix} J_{eq}^{LOVE} \\ M_{eq}^{LOVE} \end{bmatrix} = \begin{bmatrix} E_{\theta}^{REF} \\ E_{\phi}^{REF} \end{bmatrix} \quad (3.1)$$

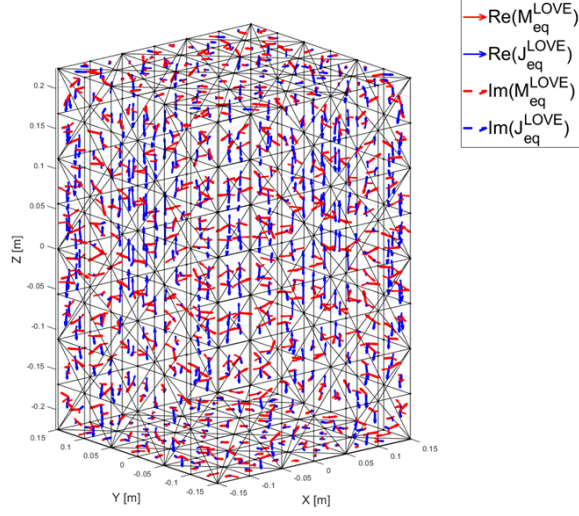


Figure 3.3. Surface density equivalent currents reconstructed on Σ_R .

Discrete electric and magnetic surface density currents by RWG basis functions:

$$\begin{cases} J_{eq}^{LOVE} = \sum_n J_n \cdot f_n \\ M_{eq}^{LOVE} = \sum_n M_n \cdot \eta_0 \cdot f_n \end{cases} \quad (3.2)$$

EJ , EM are the free-space radiation matrices. The E-field of the single radiating dipole at the center of the observed points (or sampled points) is reconstructed.

$$[E_{NF,REC}] = [EJ \quad EM] \begin{bmatrix} J_{eq}^{LOVE} \\ \eta_0 M_{eq}^{LOVE} \end{bmatrix} \quad (3.3)$$

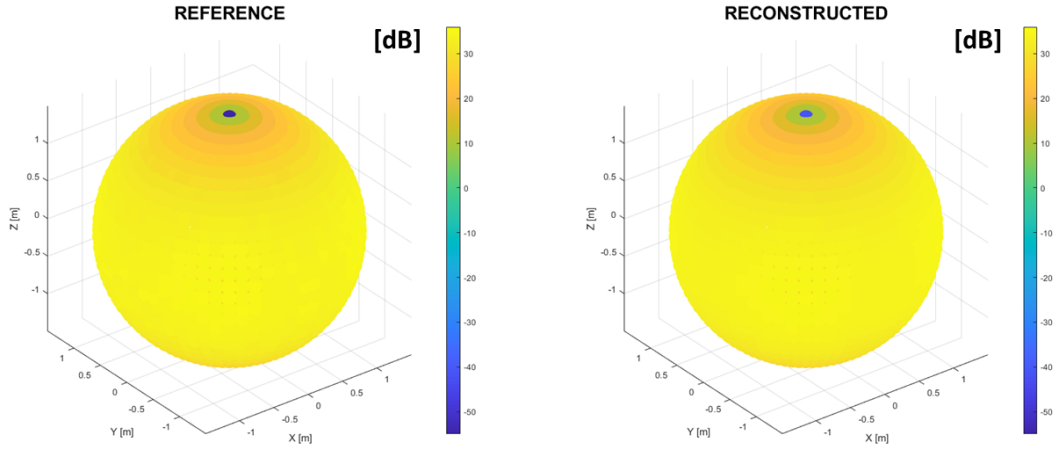


Figure 3.4. NF reference (left) and NF reconstructed (right) represented as intensity points (in dB) on a sphere with radius equal to the distance if the observation locations.

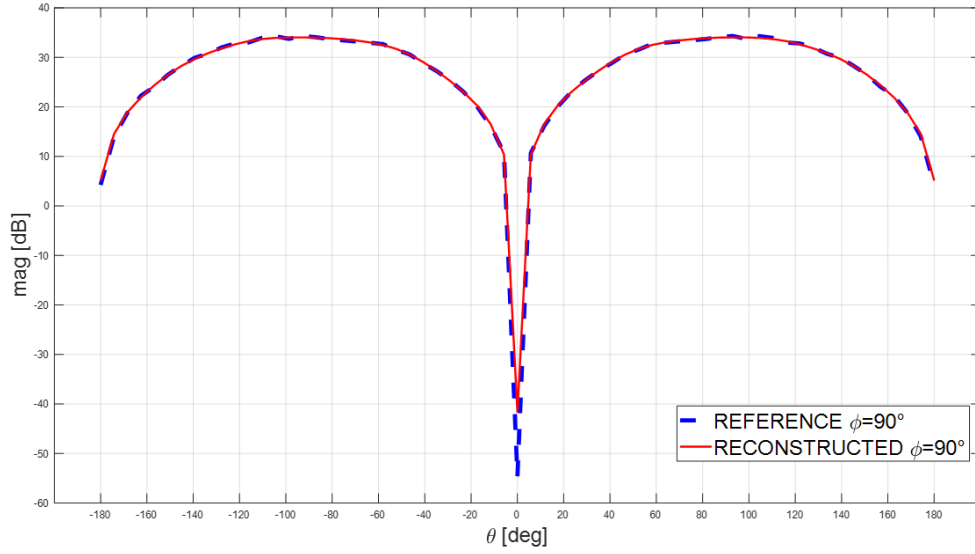


Figure 3.5. NF reference (left) and NF reconstructed (right) cuts at $\phi = 90^\circ$.

Here is reported the relative reconstruction error.

$$\Delta_e = \frac{\| \|E_{NF,REF}\| - \|E_{NF,REC}\| \|}{\|E_{NF,REF}\|} = 0.055\% \quad (3.4)$$

Now knowing the relation between NF and FF it is possible to transpose the electric

field in far-field by applying the method proposed in [3], which will be reported briefly below for the sake of clarity. The NF-to-FF transformation can be obtained from the electric current coefficients calculated at NF ($J_{eq}^{LOVE}, M_{eq}^{LOVE}$).

$$E_{0,FF}(\hat{r}) = C \int e^{jk_0 \hat{r} \cdot \underline{r}'} J(\underline{r}') d\underline{r}' \quad (3.5)$$

Then for each element it is possible to translate the FF in 3.6:

$$E_{T,FF}(\hat{r}) = C \int e^{jk_0 \hat{r} \cdot (\underline{r}' - \underline{r}_0 + \underline{r}_0)} J(\underline{r}' - \underline{r}_0) d(\underline{r}' - \underline{r}_0) \quad (3.6)$$

Applying the transformation for the electric and magnetic current coefficients, the resulting electric and magnetic radiation matrix (EJ_{FF}, EM_{FF}) are used to express the component E_θ and E_ϕ of the electric field at FF.

$$E_{FF,REC} = \sqrt{|E_\theta|^2 + |E_\phi|^2} \quad (3.7)$$

Finally exploiting the solution in 3.6 the resulting FF is reported in Figure 3, Figure 3.7 and Figure 3.8.

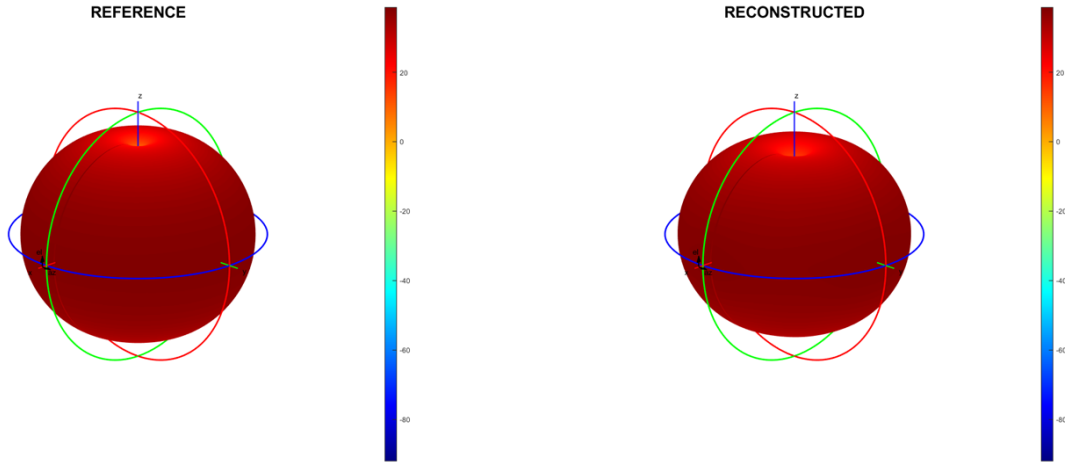


Figure 3.6. FF radiation pattern, reference (left) and reconstructed (right).

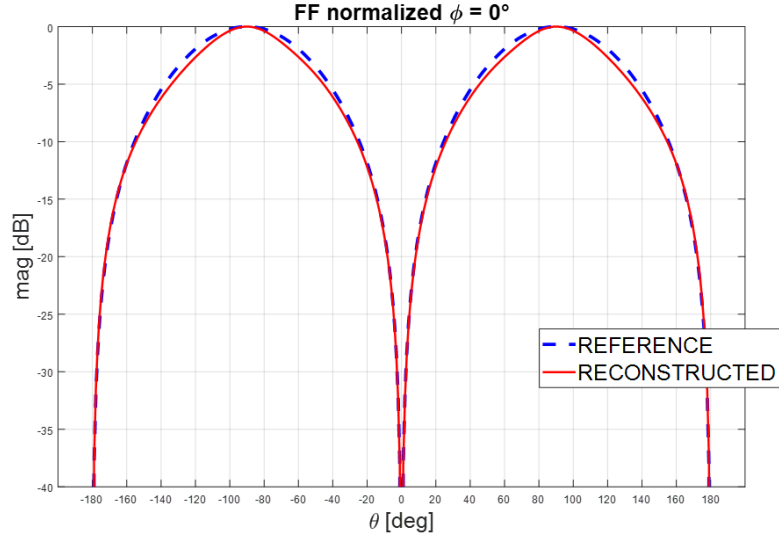


Figure 3.7. FF pattern cut at $\phi = 0^\circ$, reference (blue) and reconstructed (red).

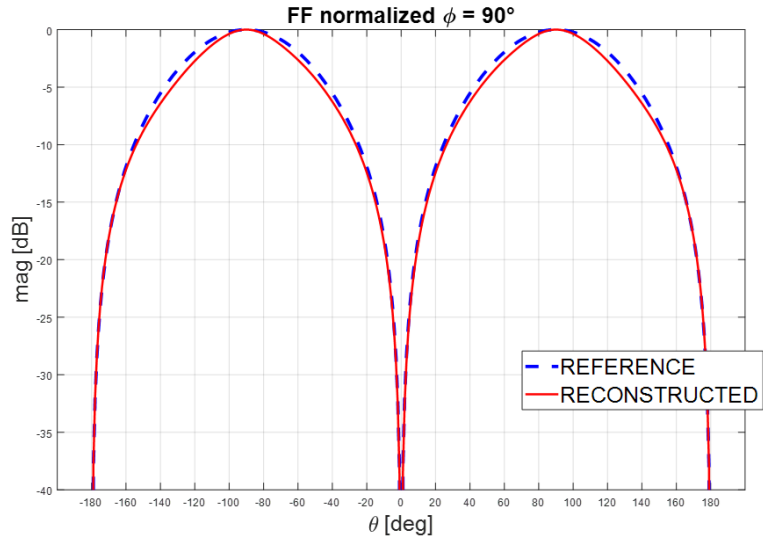


Figure 3.8. FF pattern cut at $\phi = 90^\circ$, reference (left) and reconstructed (right).

$$\Delta_e = \frac{\| \|E_{FF,REF}\| - \|E_{FF,REC}\| \|}{\|E_{FF,REF}\|} = 4.14\% \quad (3.8)$$

3.1 Dipole array reconstruction

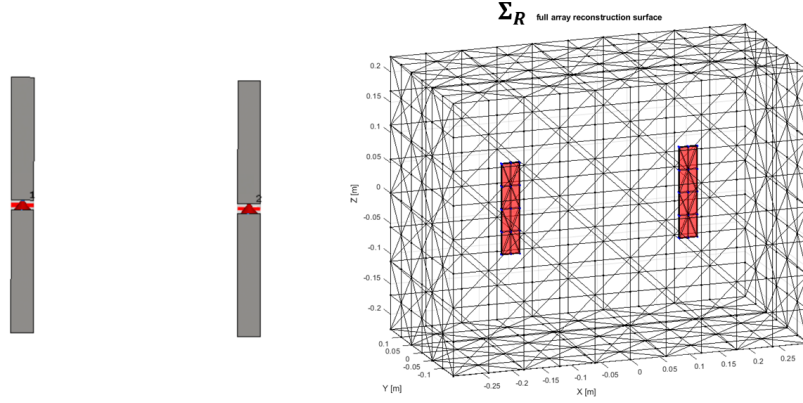


Figure 3.9. Strip dipole array model from CST simulation (left) and reconstruction surface (right).

In this section, it will be explained the main topic of this thesis, which is the reconstruction of the radiation pattern of the array from the coefficients evaluated on the single element. First of all it should be possible to translate the equivalent currents, J_{eq}^{LOVE} and M_{eq}^{LOVE} , on each element in space, or, likewise, to translate the reconstruction surface (Σ_{R1} and Σ_{R2} in Figure 3.10) in each position of the elements of the array, and then calculate their relative discrete radiation matrix (EJ_1, EJ_2, EM_1, EM_2), to apply the equivalence currents. Follows an example showing the reconstructed NF for both dipoles constituting the array elements.

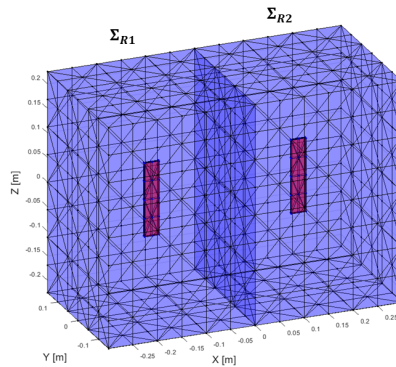


Figure 3.10. Reconstruction surfaces shifted for each element of the strip dipole array.

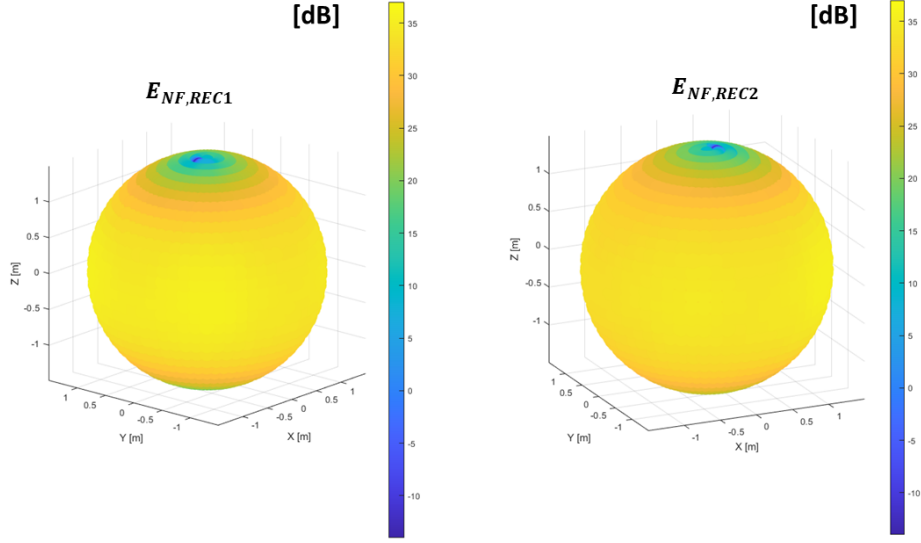


Figure 3.11. Electric field intensity for each element of the linear array.

Then for exciting each single elements, both with electric current (J) and magnetic currents (M), to consider their radiating contribution independently from each other, it was formulated the matrix defined as α_{SHIFT} .

$$[\alpha_{SHIFT}] = \begin{bmatrix} J_1 & 0 & 0 & 0 \\ 0 & 0 & J_2 & 0 \\ 0 & M_1 & 0 & 0 \\ 0 & 0 & 0 & M_2 \end{bmatrix} \quad (3.9)$$

From now on the matrix containing the equivalent currents shifted in order to excite each single array elements will be referred as α_{SHIFT} , and it will have $2N$ columns with N the number of array elements. The new coefficients $\alpha_1, \dots, \alpha_4$ have been solved in least-square sense:

$$[EJ_1 \quad EJ_2 \quad EM_1 \quad EM_2] [\alpha_{SHIFT}] [\alpha_1, \dots, \alpha_4] = \begin{bmatrix} E_{NF,REF}^\theta \\ E_{NF,REF}^\phi \end{bmatrix} \quad (3.10)$$

Then they were used to reconstruct the array NF. The results are shown in Figure 3.12 and Figure 3.13.

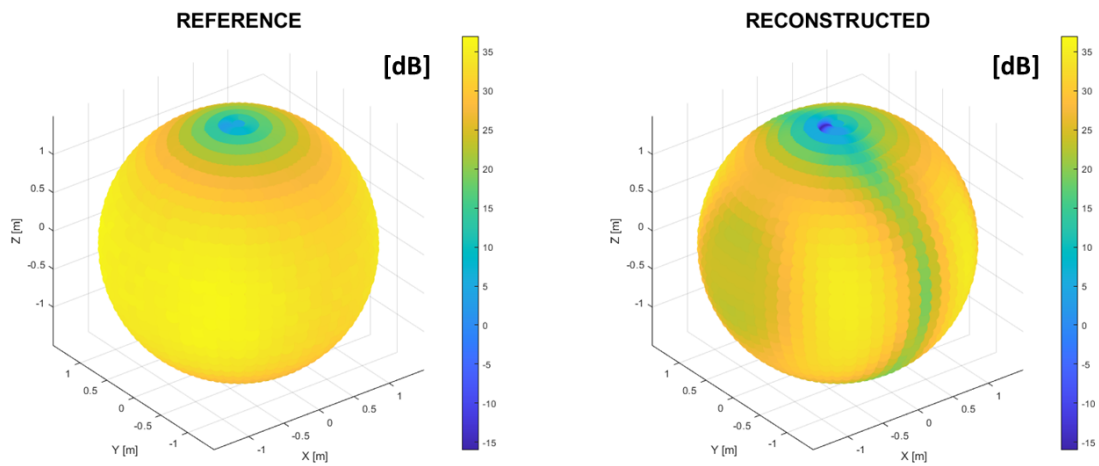


Figure 3.12. Electric field intensity of the linear array, reference NF (left) and reconstructed NF (right).

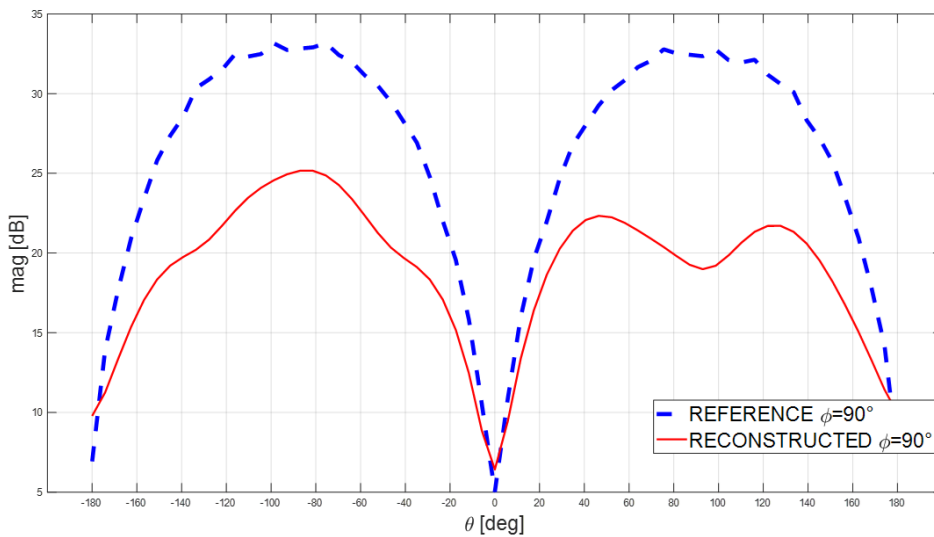


Figure 3.13. Electric field pattern of the linear array at $\phi = 90^\circ$, reference NF (blue) and reconstructed NF (red).

3.2 Auxiliary sources

3.2.1 NF difference

Looking at the previous results it seems that the reconstruction error is much higher compared to the single patch case. This could be due to the radiated fields in the Beam Forming Network (BFN). In order to compensate for possible BFN dispersion and reconstruction error, it was analyzed the difference between the measured electric field, $E_{NF,REF}$, and the reconstructed electric field, $E_{NF,REC}$.

$$E_{NF,DIFF} = (E_{NF,REF}^{\theta} - E_{NF,REC}^{\theta}) \cdot \hat{\theta} + (E_{NF,REF}^{\phi} - E_{NF,REC}^{\phi}) \cdot \hat{\phi} \quad (3.11)$$

Applying the inverse-source using as reconstruction surface the rectangle in Figure 3.9, which contains all the antenna array elements, it was possible to compute the equivalent current J_{eq}^{DIFF} , M_{eq}^{DIFF} and reconstruct the electric field difference.

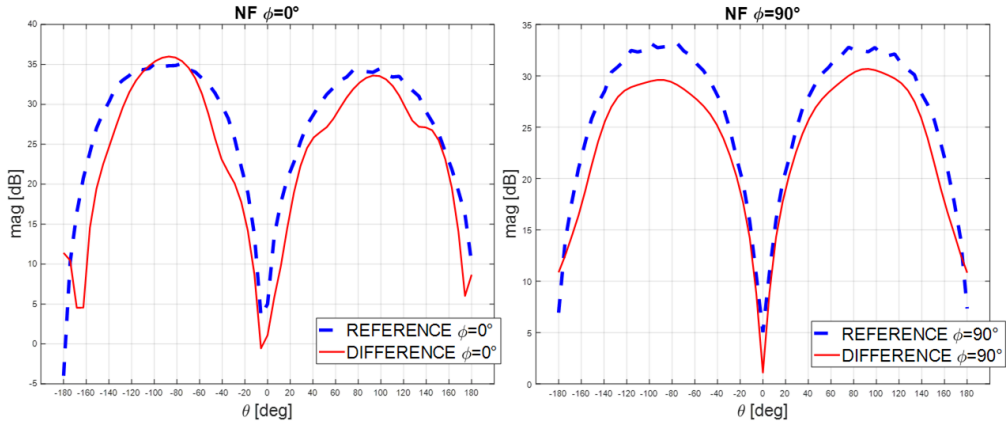


Figure 3.14. Electric field difference with the reference.

Figure 3.14 shows the current hotspots¹ from the reconstructed field $E_{NF,DIFF}$, which may represent the reconstruction error of the linear array.

¹The term hotspots refer to the region on the surface where the currents present the highest values.

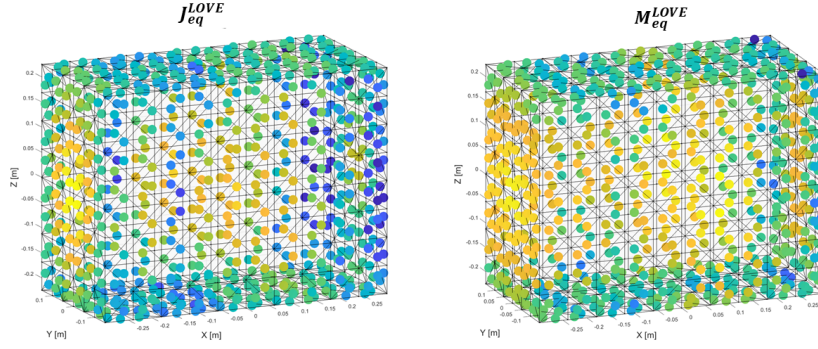


Figure 3.15. J (electric) and M (magnetic) current hotspots represented as colored points on the reconstruction surface for the entire dipole array.

Now, before proceeding to the next step and implementing the auxiliary sources, it is necessary to verify that the exact electric field of the 4-element linear array can be obtained from the sum of the electric field reconstructed by shifting the equivalent currents, and the electric field difference, in the near-field.

$$E_{NF,REF} \approx (E_{NF,DIFF}^{\theta} + E_{NF,REC}^{\theta}) \cdot \hat{\theta} + (E_{NF,DIFF}^{\phi} + E_{NF,REC}^{\phi}) \cdot \hat{\phi} \quad (3.12)$$

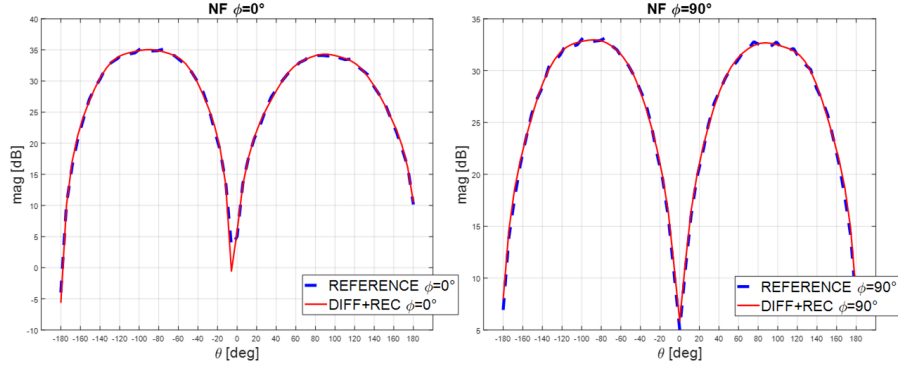


Figure 3.16. Sum between the electric field difference with the reconstructed electric field, at NF, to confirm the reconstruction error.

The sum gave a good result, then it should be possible to compensate for the reconstruction error with auxiliary sources on the perimeter of the reconstruction surface of the linear array.

3.2.2 Auxiliary sources

The objective is to enlarge the linear space of expansion functions whose coefficients have to be determined in the discrete linear system of equations to facilitate the coefficient solution via the least-square method. The reconstruction with additional sources should be addressed in the following way:

$$[[EJ, EM] [\alpha_{SHIFT}] [\alpha_1, \dots, \alpha_4], [EJ_{AUX}, EM_{AUX}]] [\alpha] = \begin{bmatrix} E_{NF,REF}^\theta \\ E_{NF,REF}^\phi \end{bmatrix} \quad (3.13)$$

with $EJ = EJ_1, EJ_2, EM = EM_1, EM_2$ and $EJ_{AUX} = EJ_{AUX,1}, \dots, EJ_{AUX,N}, EM_{AUX} = EM_{AUX,1}, \dots, EM_{AUX,N}$, N the number of auxiliary sources.

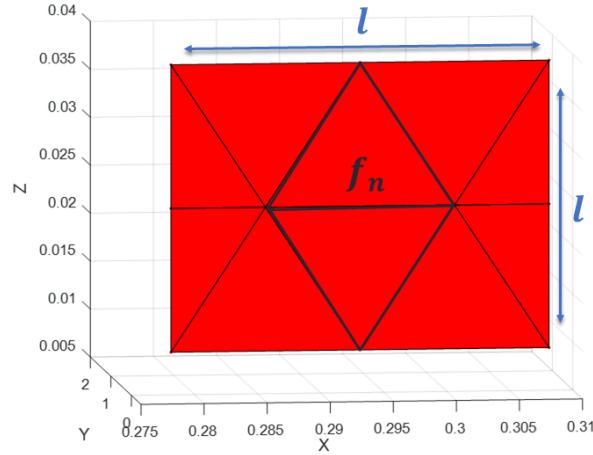


Figure 3.17. Representation of a singular auxiliary source constituted by 11 RWG basis functions, l is the sources dimension and is equal to $\lambda/5$.

The source was placed around the AUT following the dimension of the reconstruction surface for the full array antenna (Figure 3.9) in such a way to cover all the sides equally. Running the inverse-source code for the N auxiliary sources to obtain the N radiation matrix defined as EJ_n^{AUX}, EM_n^{AUX} , where n is the n -th auxiliary source and performing the least square element to find the coefficients defined as α_{AUX} , it gives an accurate reconstruction of the NF of the dipole array with acceptable relative error.

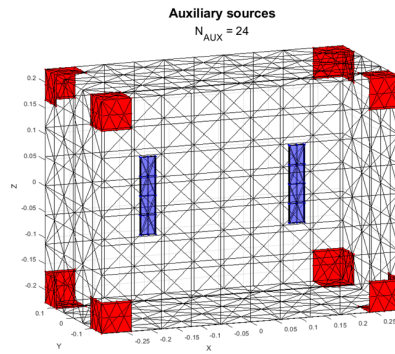


Figure 3.18. Representation of a distribution of auxiliary sources (red) around the array. $N_{AUX} = 24$.

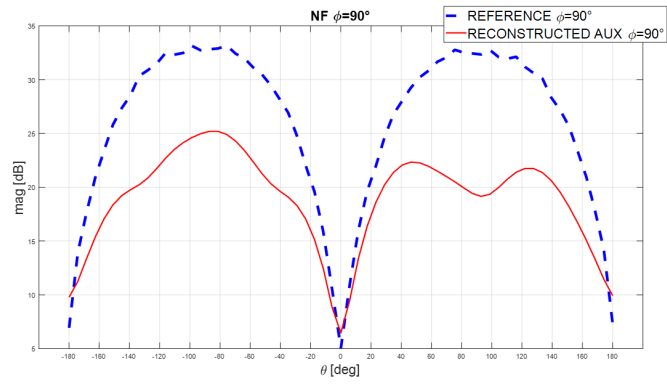


Figure 3.19. E-field reconstruction with 24 auxiliary sources at $5 \cdot 10^{-4}$ tolerance.

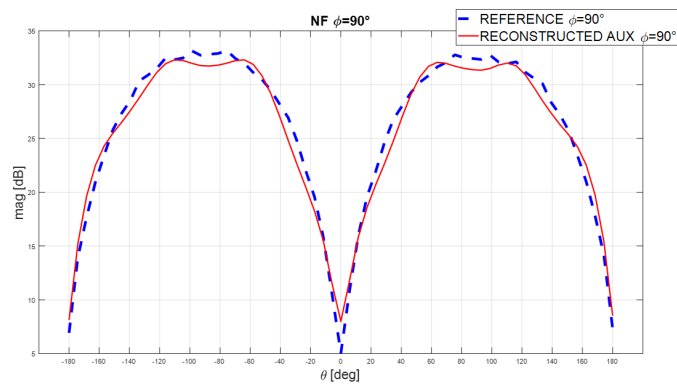


Figure 3.20. E-field reconstruction with 24 auxiliary sources at 10^{-6} tolerance.

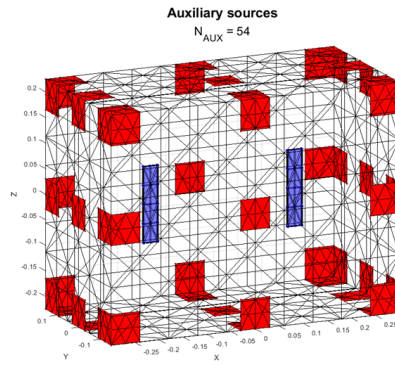


Figure 3.21. Representation of a distribution of auxiliary sources (red) around the array. $N_{AUX} = 54$.

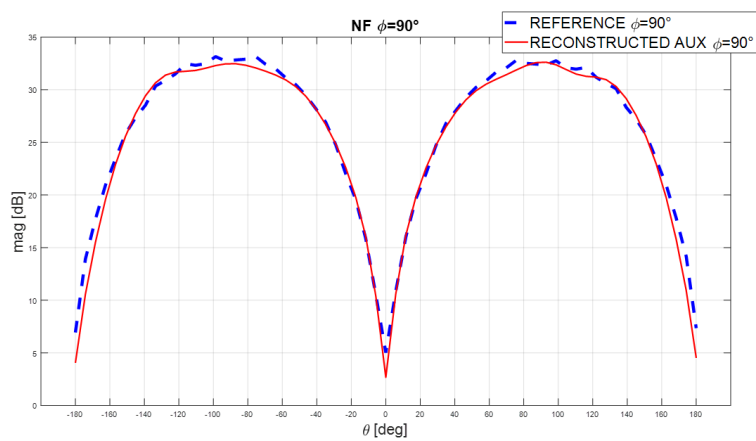


Figure 3.22. E-field reconstruction with 54 auxiliary sources for a given tolerance of 10^{-6} .

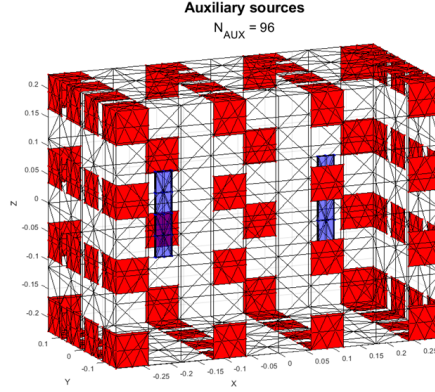


Figure 3.23. Representation of a distribution of auxiliary sources (red) around the array. $N_{AUX} = 96$.

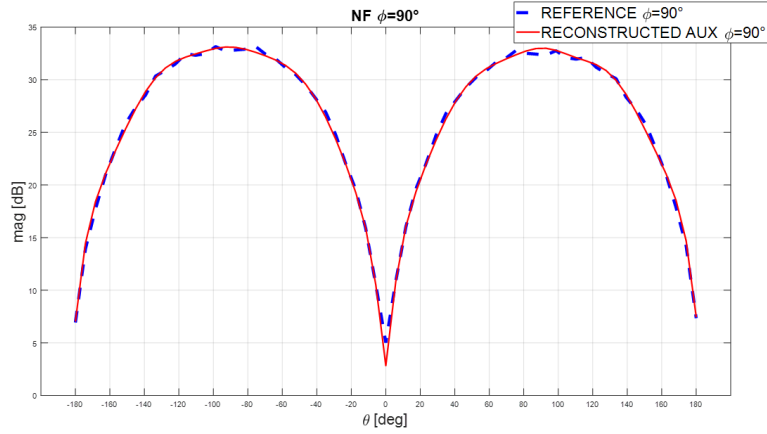


Figure 3.24. E-field reconstruction with 96 auxiliary sources for a given tolerance of 10^{-6} .

N_{AUX}	auxiliary source reconstruction
24	$\Delta_e = 0.28\%$, tol = $5 \cdot 10^{-4}$
24	$\Delta_e = 0\%$, tol = 10^{-6}
54	$\Delta_e = 0.1\%$, tol = 10^{-6}
96	$\Delta_e = 0.008\%$, tol = 10^{-6}

Table 3.1. Comparison between different distribution of auxiliary sources for the FF reconstruction of the linear array.

3.3 FF reconstruction methods comparison

The method proposed in this thesis seems to work in the case of a strip dipole array which is a very ideal one. Also, the number of sampled points used in this reconstruction (1953 samples) is much more than necessary to represent the array far-field. Thus it is expected that the reconstruction error for the direct inverse-source method (i.e. applying the method proposed for the reconstruction of the single element but using the full array) will present the best reconstruction error due to the elevated number of points.

All three methods for the reconstruction of the 2×1 strip dipole array electric field are reported below to compare their reconstruction error Δ_e .

- inverse-source linear array

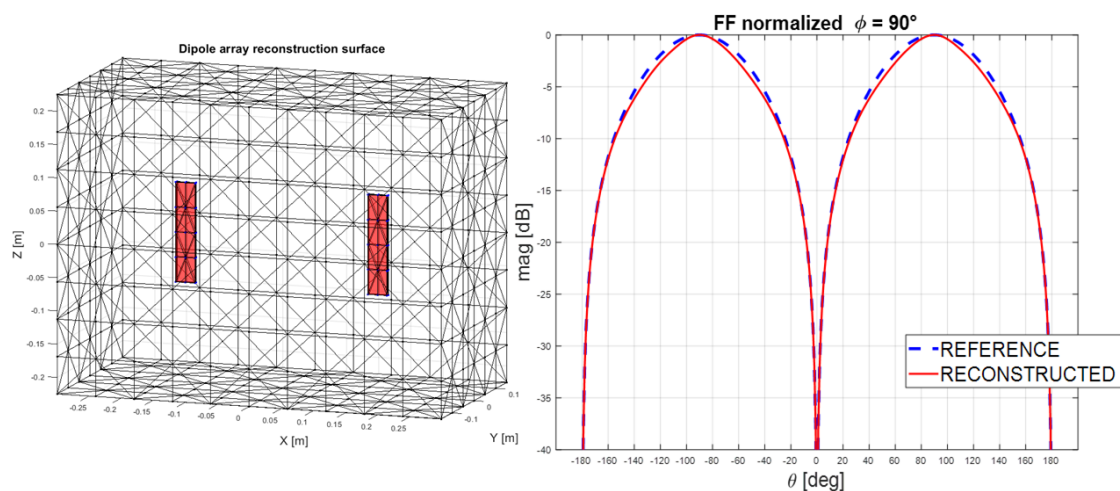


Figure 3.25. Direct inverse-source reconstruction of the entire array, reconstruction surface (left) and FF cut at $\phi = 90^\circ$ (right).

- reconstruction without auxiliary sources

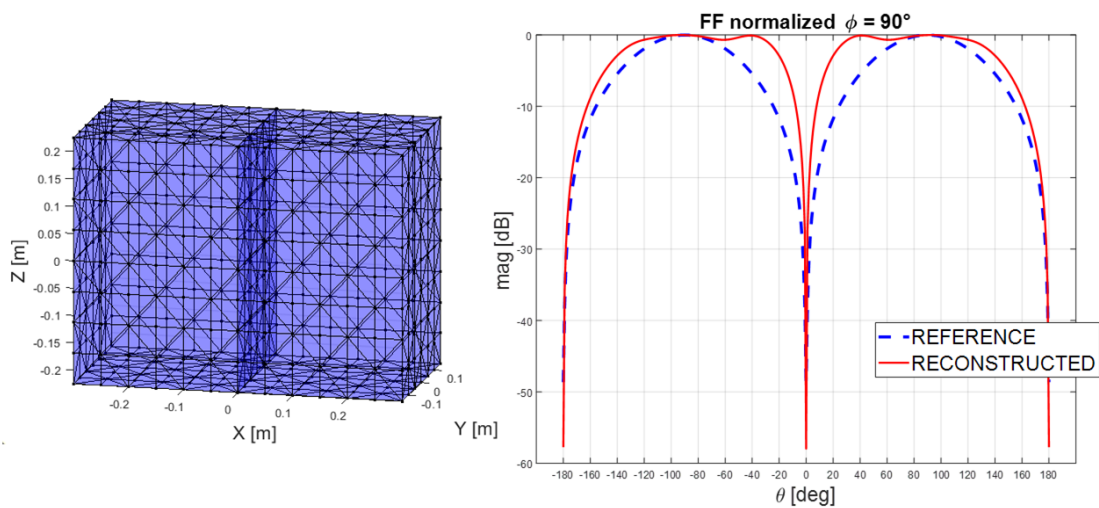


Figure 3.26. Reconstruction only by translating the reconstruction surface, Σ_{R1}, Σ_{R2} (left), and FF reconstructed at $\phi = 90^\circ$ (right).

- reconstruction with auxiliary sources

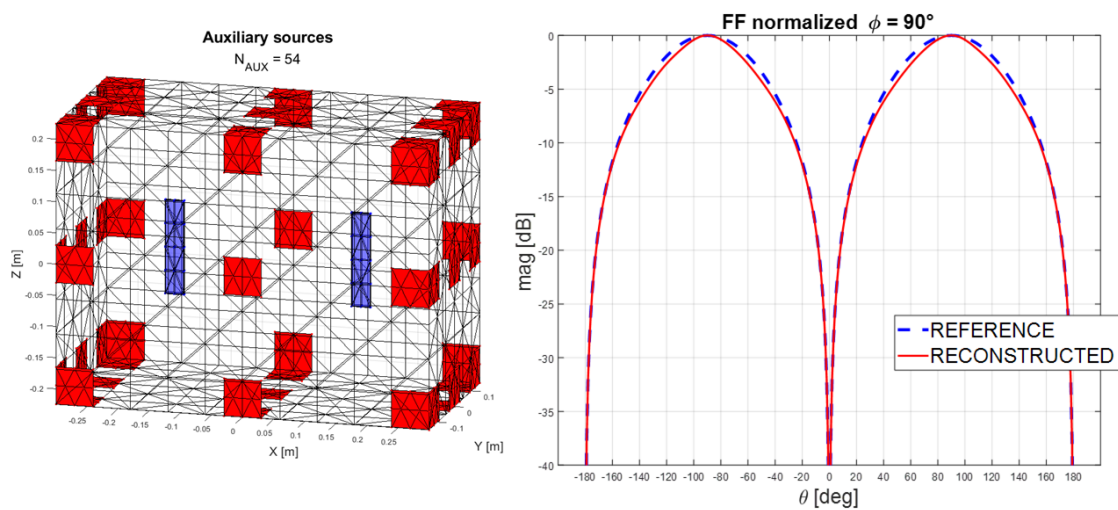


Figure 3.27. Reconstruction with auxiliary sources. Sources distribution (left) and FF cut at $\phi = 90^\circ$ (right).

To summarise the results obtained in this chapter are presented in the table below and as was expected, in this case, the inverse-source method applied to a surface enclosing the entire array presents the best results.

Nevertheless, with the reconstruction using auxiliary sources, which is the main method proposed by this thesis, it was possible to achieve a very similar reconstruction error. This comparison will be presented also in the next chapter with the reconstruction of a real patch antenna array without the over-sampled number of points chosen in this case but with the minimum number of points necessary to represent only one element. Then the comparison between reconstruction methods will be more appropriate.

method	FF reconstruction
inverse-source	$\Delta_e = 3.87\%$, tol = 10^{-6}
translating Σ_R	$\Delta_e = 9.01\%$, tol = 10^{-6}
with auxiliary sources	$\Delta_e = 4.54\%$, tol = 10^{-6}

Table 3.2. Comparison between different distribution of auxiliary sources for the FF reconstruction of the linear array.

Chapter 4

Antenna Array Reconstruction

The objective of this chapter will be to obtain a reasonable reconstruction of the single element FF radiation pattern (in terms of relative reconstruction error and pattern shape) with the minimum number of sampled points for the single element. Then the information extrapolated from the aforementioned reconstruction it was used as a base for the characterization of the full array radiation pattern, as already seen in chapter 3. After that, there will be presented also a reconstruction with the minimum number of points needed for the representation of the full array structure (4 patch antennas and BFN).

4.1 Antenna design

W	147 mm
L	147 mm
h	1.5 mm
t	0.1 mm
ϵ_r	1
f_0	1 GHz
d	239.83 mm

Table 4.1. Antenna design parameters.

The design of an antenna linear array with 4 equi-spaced elements. The simulations from this structure will be used as reference for the reconstruction of the entire field radiation pattern from the single element in Figure 4.1.

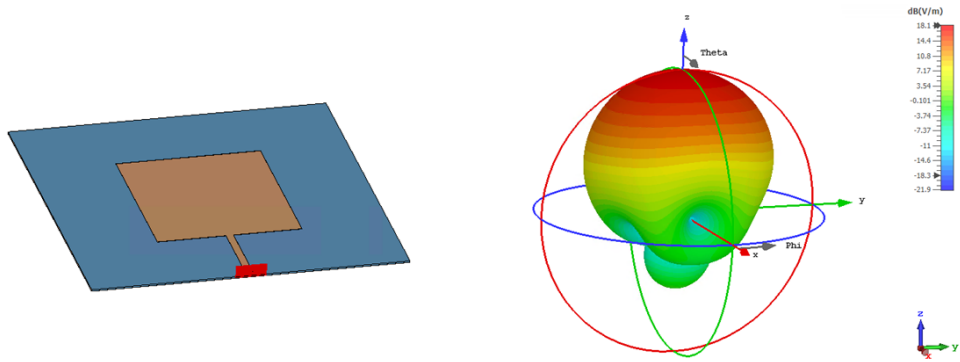


Figure 4.1. Single patch antenna structure (left) and electric field radiation pattern in far field (right).

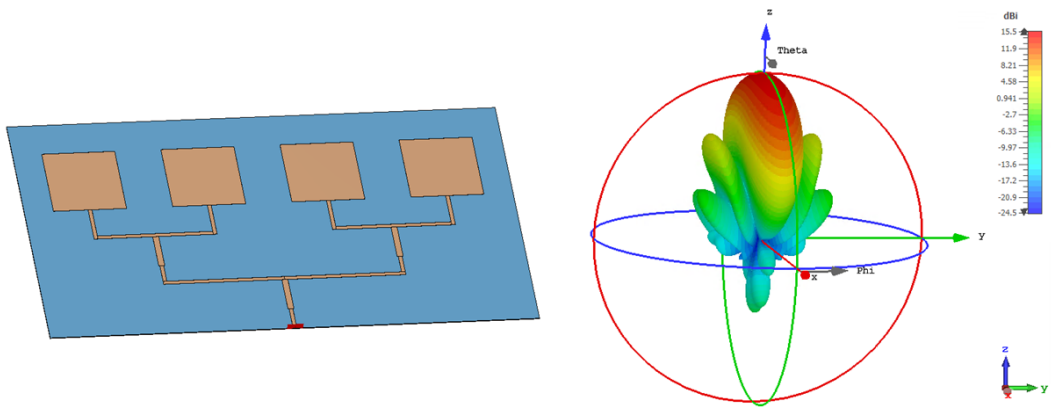


Figure 4.2. Linear array antenna structure (left) and electric field radiation pattern in far field (right).

4.1.1 Subsampling

The minimum number of sampling points is defined as a function of the minimum sphere which contains the antenna element as:

$$N = \lceil \frac{4\pi R^2}{(\lambda/2)^2} \rceil \quad (4.1)$$

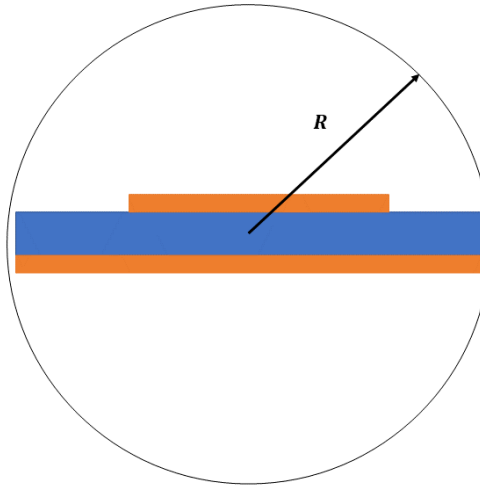


Figure 4.3. Minimum sphere around the AUT.

In table 4.2 are reported the number of sampling points chosen from the formula in 4.1 to characterize the reconstruction problems.

N	theory (eq.4.1)	CST export
PATCH	28	28
ARRAY	177	190

Table 4.2. Minimum number of sampling points from theoretical formula and the actual sampling points exported from CST.

In the next sections, it will be presented the same reconstruction process used in chapter 3 for the strip dipole array applied at the patch antenna array in Figure 4.1, for 28 sampled points, and 190 sampled points. Both reconstructions were performed using the E-field exported from the CST simulations at a distance of 5λ from the AUT, which is equal to 1.499 m.

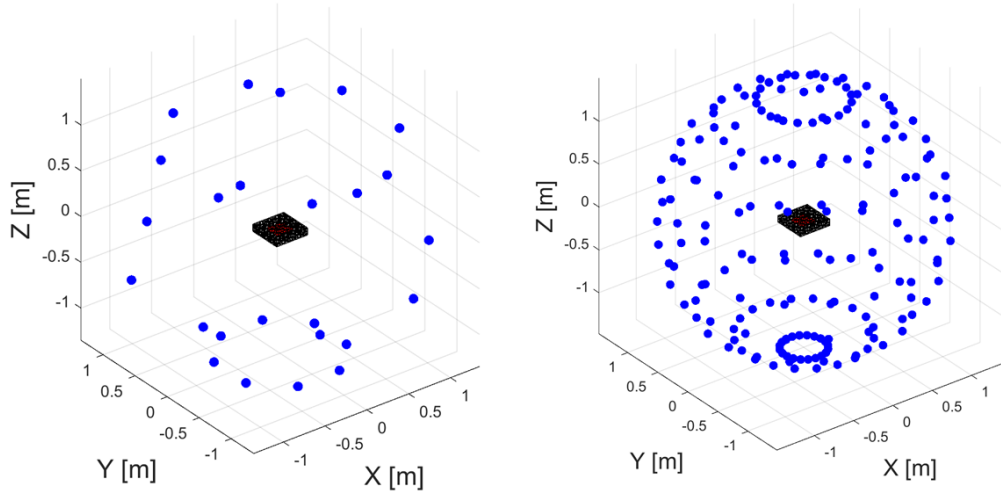


Figure 4.4. Sampled point around the microstrip patch antenna, at distance 5λ , reported in MATLAB. 28 points (left), 190 points (right).

4.2 Reconstruction with 28 points

Here is presented the surface reconstruction (Σ_R) for the single element: a microstrip patch antenna.

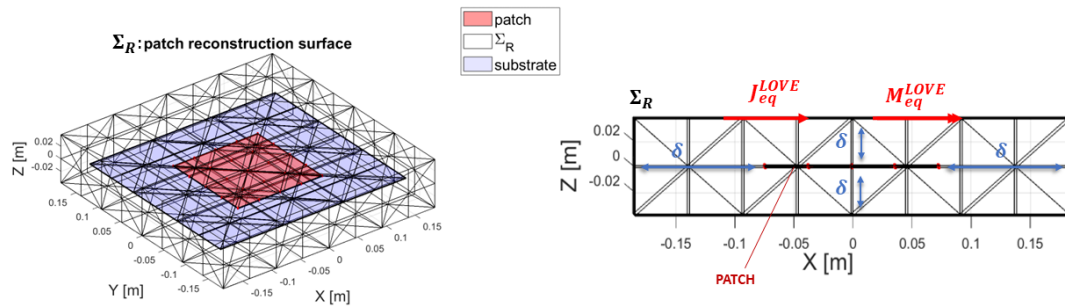


Figure 4.5. Single patch reconstruction surface (Σ_R), δ is the gap, in red the actual dimension of the metal patch, and in blue the dimension of the substrate.

Before proceeding into the reconstruction, having a limited amount of samples, it must be discussed the characterization of the reconstruction surface, more specifically its geometry and implicitly its area. The area of the surface $A(\Sigma_R)$ in the representation in Figure 4.1 is in function of the parameter δ . From the work discussed in [7], it results that the complexity of the reduced-order model and consequently the number of unknowns is given by the area of the reconstruction surface around the AUT. Defining N as the number of sampling needed for an accurate FF representation:

$$N = \frac{A(\Sigma_R)}{(\lambda/2)^2} \quad (4.2)$$

it is then easily deduced that the complexity of the FF reconstruction problem can be simplified by decreasing the area of the surface Σ_R . This particular attention to the first steps of the process is given because the accurate characterization of the single element is been noted to be of particular relevance in the outcome of the final result. The lower the error of the single element FF reconstruction, the lower the relative error of the array reconstruction. It was performed an analysis changing the value of δ to verify the statement discussed in [7].

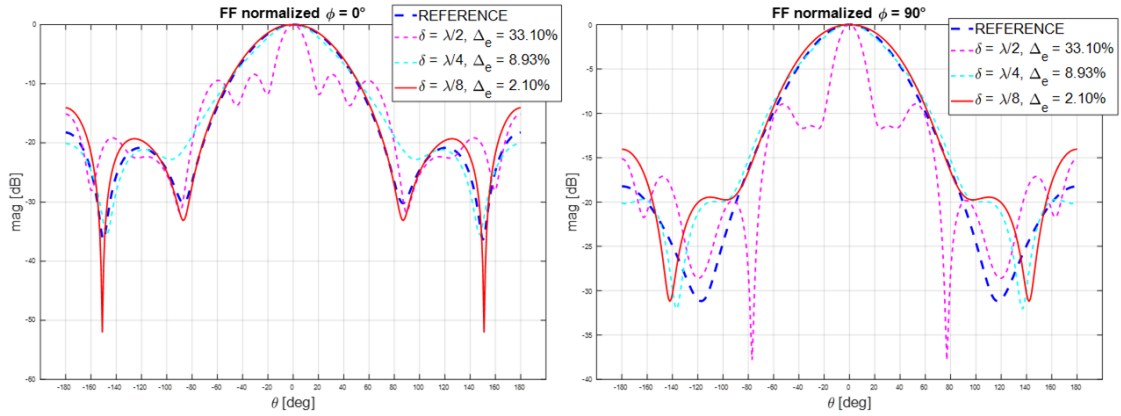


Figure 4.6. Representation at the two main cut $\phi = 0^\circ$, $\phi = 90^\circ$

As a result, the statement has found to be applicable even in this case and it was selected the value of $\delta = \lambda/8$ (i.e. the one that gives the smaller area $A(\Sigma_R)$) for a reconstruction error of the FF of 2.10%. The relative NF reconstruction is reported in Figure 4.6 with a relative reconstruction error of 0.037%.

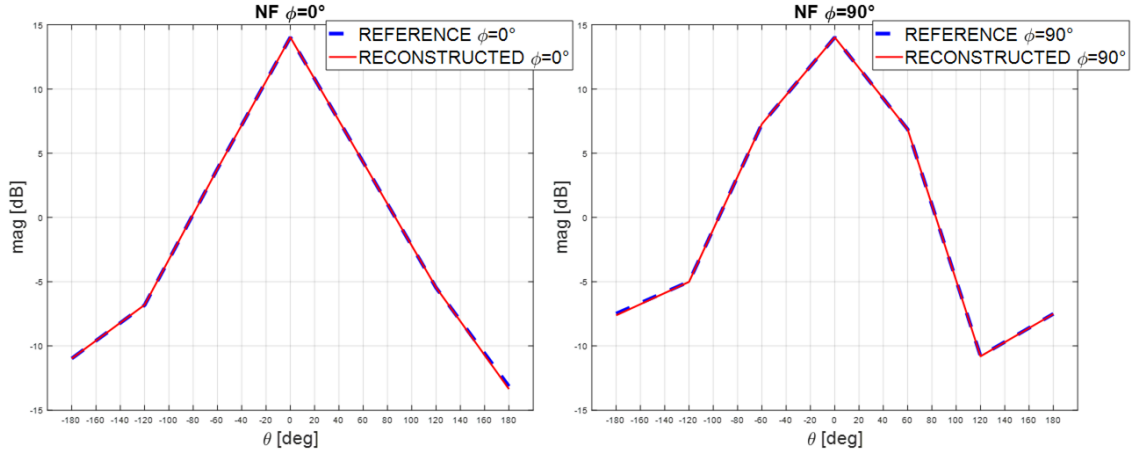


Figure 4.7. Representation at the two main cut $\phi = 0^\circ$, $\phi = 90^\circ$

4.2.1 Linear array reconstruction

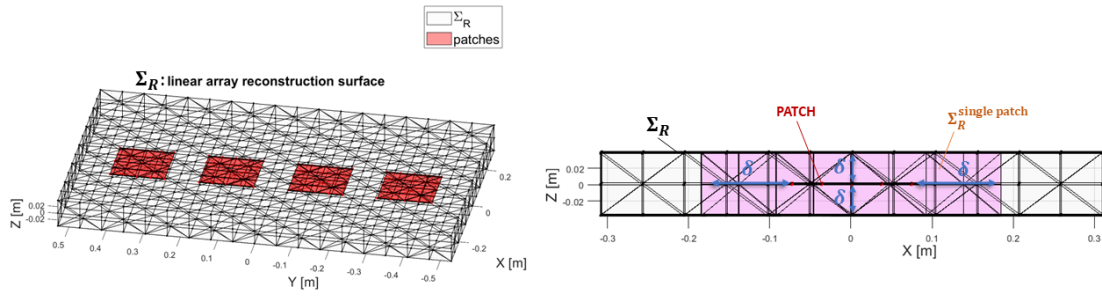


Figure 4.8. Linear array reconstruction surface (Σ_R).

The reconstruction of the linear array is addressed. As explained in chapter 3 for the reconstruction of the strip dipole array, the idea is to calculate the NF for each element by shifting the reconstruction surface Σ_R , calculating the radiation matrix on each position

and then using the surface density coefficients evaluated in the previous section, from the single microstrip patch antenna, to characterize each individual element radiation pattern. This is basically the "a-priori" knowledge of the antenna that can be used to compensate for the missing information due to under-sampling with respect to the linear array dimension (i.e. using 28 sampling points to represent the radiation pattern in FF of an antenna which needs at least ≈ 177 points). In Figure 4.9 is represented each element of the linear array with its relative reconstruction surface and the electric and magnetic currents on their surface.

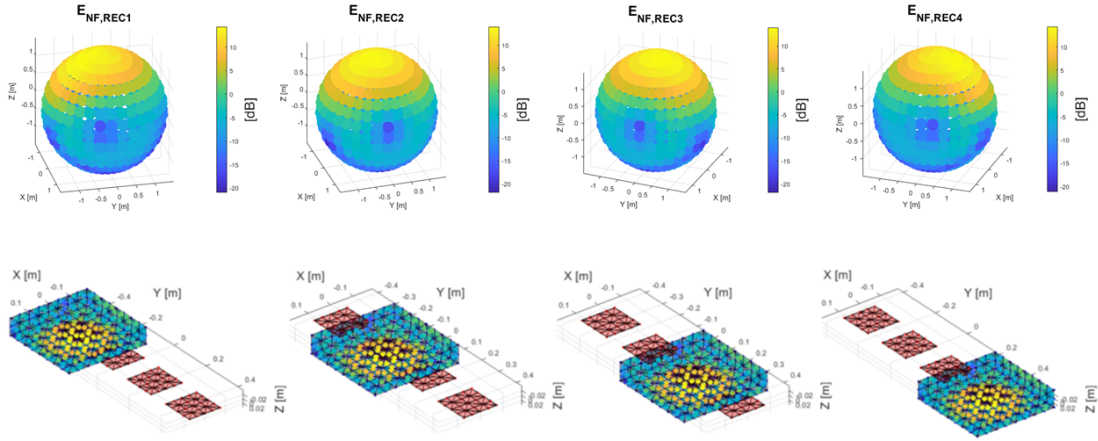


Figure 4.9. Representation of each single element reconstruction surface and their relative reconstructed surface currents ($J_{eq}^{LOVE}, M_{eq}^{LOVE}$), and the reconstructed near fields $E_{NF,RECn}$, with n as the number of element in the array.

In Figure 4.10 and Figure 4.11 are reported the results obtained only by translation of the reconstruction surface using the coefficients evaluated from the single element.

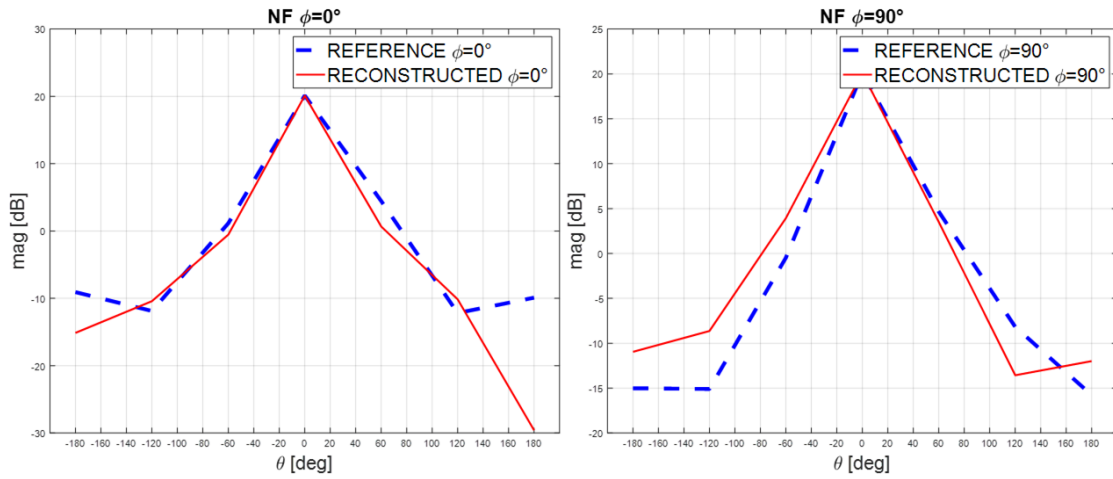


Figure 4.10. E-field NF reconstruction only by translation, of the linear array, cuts at $\phi = 0^\circ$ and $\phi = 90^\circ$.

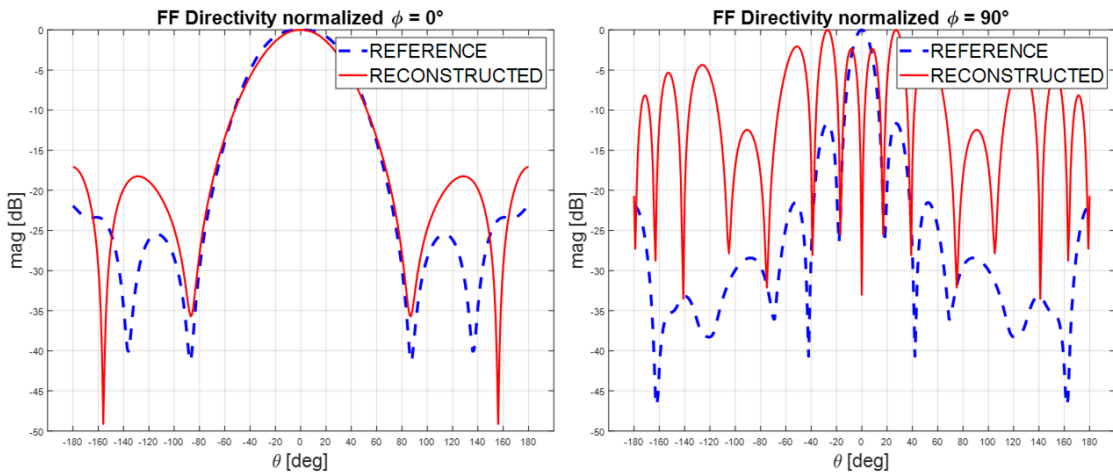


Figure 4.11. E-field FF reconstruction only by translation, of the linear array, cuts at $\phi = 0^\circ$ and $\phi = 90^\circ$.

Here are the relative matrix operations. The coefficients $\alpha_1, \dots, \alpha_8$ are obtained applying the least square method with respect to the reference NF of the linear array.

$$\begin{bmatrix} EJ_1^\theta & \dots & EJ_4^\theta & EM_1^\theta & \dots & EM_4^\theta \\ EJ_1^\phi & \dots & EJ_4^\phi & EM_1^\phi & \dots & EM_4^\phi \end{bmatrix} \begin{bmatrix} J_1 & 0 & \dots & 0 & 0 \\ 0 & 0 & \dots & 0 & 0 \\ 0 & 0 & \dots & 0 & 0 \\ 0 & 0 & \dots & J_4 & 0 \\ 0 & M_1 & \dots & 0 & 0 \\ 0 & 0 & \dots & 0 & 0 \\ 0 & 0 & \dots & 0 & 0 \\ 0 & 0 & \dots & 0 & M_4 \end{bmatrix} [\alpha_1 \quad \dots \quad \alpha_8] = \begin{bmatrix} E_{NF,REF}^\theta \\ E_{NF,REF}^\phi \end{bmatrix} \quad (4.3)$$

$$\alpha_{SHIFT} = \begin{bmatrix} J_1 & 0 & \dots & 0 & 0 \\ 0 & 0 & \dots & 0 & 0 \\ 0 & 0 & \dots & 0 & 0 \\ 0 & 0 & \dots & J_4 & 0 \\ 0 & M_1 & \dots & 0 & 0 \\ 0 & 0 & \dots & 0 & 0 \\ 0 & 0 & \dots & 0 & 0 \\ 0 & 0 & \dots & 0 & M_4 \end{bmatrix} \quad (4.4)$$

The radiation matrices in FF are already evaluated considering the Love's coefficients, so in order to sum each effect independently it was used a unitary "shifting matrix" is defined as:

$$\alpha_{SHIFT}^u = \begin{bmatrix} 1 & 0 & \dots & 0 & 0 \\ 0 & 0 & \dots & 0 & 0 \\ 0 & 0 & \dots & 0 & 0 \\ 0 & 0 & \dots & 1 & 0 \\ 0 & 1 & \dots & 0 & 0 \\ 0 & 0 & \dots & 0 & 0 \\ 0 & 0 & \dots & 0 & 0 \\ 0 & 0 & \dots & 0 & 1 \end{bmatrix} \quad (4.5)$$

Then the reconstructed FF only by translation of each single element radiation matrix was obtained from the following equation:

$$E_{FF,REC} = \begin{bmatrix} EJ_{FF1}^\theta & \dots & EJ_{FF4}^\theta & EM_{FF1}^\theta & \dots & EM_{FF4}^\theta \\ EJ_{FF1}^\phi & \dots & EJ_{FF4}^\phi & EM_{FF1}^\phi & \dots & EM_{FF4}^\phi \end{bmatrix} [\alpha_{SHIFT}^u][\alpha_1, \dots, \alpha_8] \quad (4.6)$$

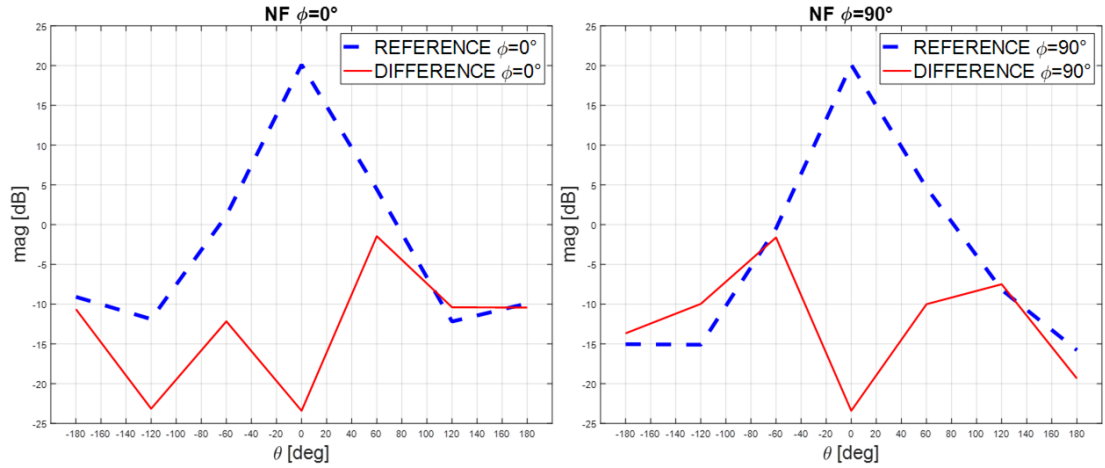
Acronym	Explanation
J_{eq}^{LOVE}	Equivalent surface electric current
M_{eq}^{LOVE}	Equivalent surface magnetic current
$E_{NF,REF}$	electric field near-field reference
$E_{NF,REC}$	electric field near-field reconstructed
$E_{FF,REF}$	electric field far-field reference
$E_{FF,REC}$	electric field far-field reconstructed
$[\alpha]$	unknown coefficients in the least mean square system of equations

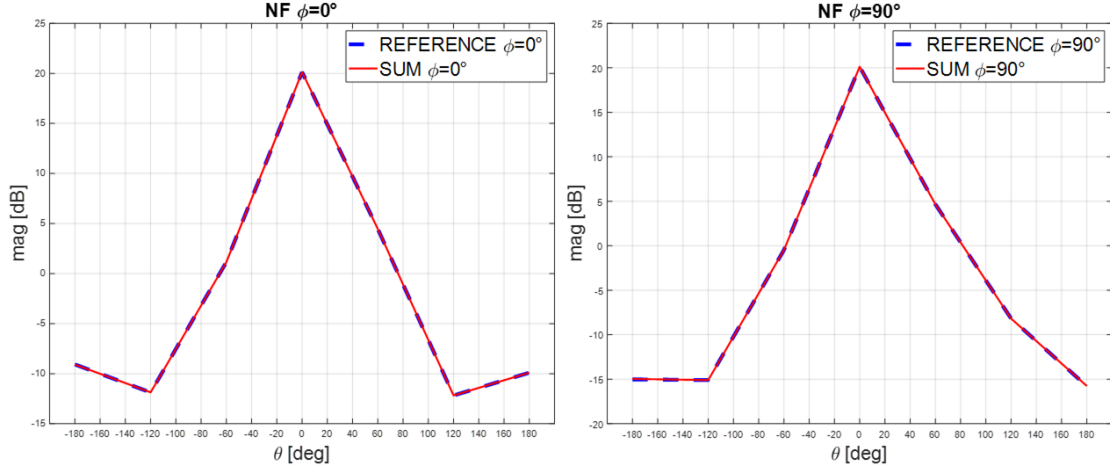
Table 4.3. List of acronyms used in the reconstruction equations.

4.2.2 Auxiliary sources

For a better approximation of the antenna array radiation pattern, it is necessary to add auxiliary sources that compensate for the reconstruction error coming from the error in the single element FF reconstruction and possible BFN leakages. The reconstruction with auxiliary sources is already been discussed in the strip dipole case in chapter 3. Here is reported the electric field difference $E_{NF,DIFF}$ and the sum to verify the process feasibility. Then some auxiliary source distributions are presented with their reconstructed fields and discussed.

$$E_{NF,REF} \approx E_{NF,REC} + E_{NF,DIFF} \quad (4.7)$$


 Figure 4.12. E-field NF difference of the linear array, cuts at $\phi = 0^\circ$ and $\phi = 90^\circ$.


 Figure 4.13. E-field NF sum, cuts at $\phi = 0^\circ$ and $\phi = 90^\circ$.

$N_{AUX} = 64$	704 basis functions	$\Delta_e = 4.83\%$
$N_{AUX} = 42$	462 basis functions	$\Delta_e = 5.61\%$
$N_{AUX} = 16$	176 basis functions	$\Delta_e = 7.73\%$

Table 4.4. Auxiliary sources and their relative FF reconstruction error.

There have been studied three cases reported in Table 4.4 with the resulting relative reconstruction errors. It must be said that for the solution of the coefficients $[\alpha]$ which represent the reconstructed NF of the linear array as:

$$\left[\left[EJ, EM \right] \left[\alpha_{SHIFT} \right] \left[\alpha_1, \dots, \alpha_8 \right], \left[EJ_{AUX}, EM_{AUX} \right] \right] [\alpha] = \begin{bmatrix} E_{NF,REF}^\theta \\ E_{NF,REF}^\phi \end{bmatrix} \quad (4.8)$$

with $EJ = EJ_1, \dots, EJ_4$, $EM = EM_1, \dots, EM_4$ and $EJ_{AUX} = EJ_{AUX,1}, \dots, EJ_{AUX,N}$, $EM_{AUX} = EM_{AUX,1}, \dots, EM_{AUX,N}$, N the number of auxiliary sources. It was used the least square method in MATLAB (**lsqr** function) with a fixed tolerance of 10^{-2} . Due to the complexity of the radiation pattern of the AUT, lower tolerances lead to increasing errors in the FF reconstruction, instead, they work fine at NF. For the strip dipole case, there was no problem in the FF reconstruction even at 10^{-6} tolerance. This could be due to the shape of its pattern, hence the problem unknowns, which is less complex with respect to a patch antenna. The results presented in this chapter will be all considered with a tolerance of 10^{-2} giving an acceptable value of residual after the application of the least mean square algorithm.

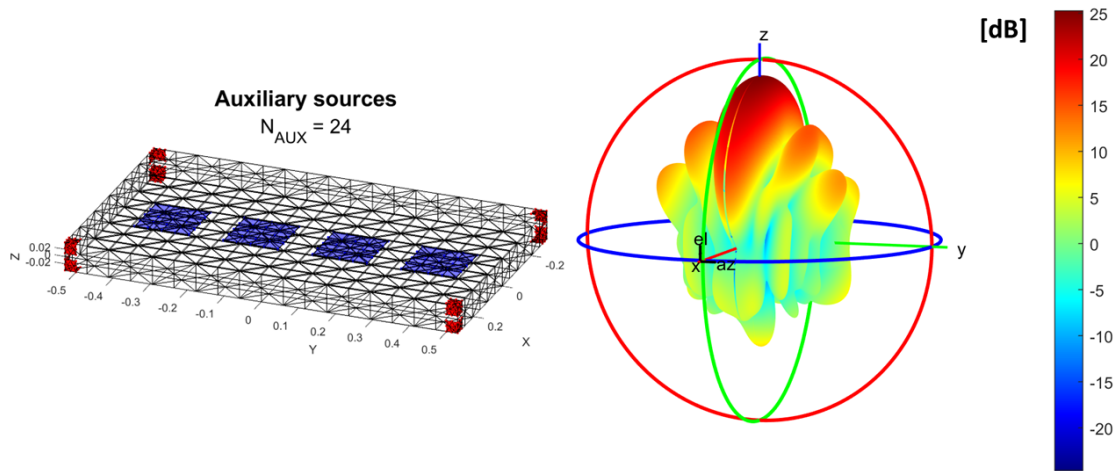


Figure 4.14. Distribution of 24 auxiliary sources around the linear array (left), FF pattern reconstructed (right).

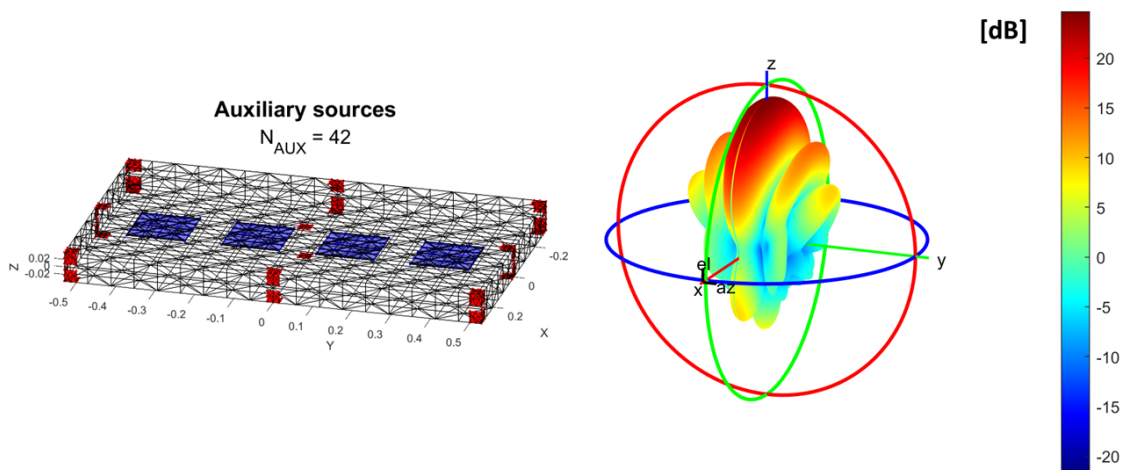


Figure 4.15. Distribution of 42 auxiliary sources around the linear array (left), FF pattern reconstructed (right).

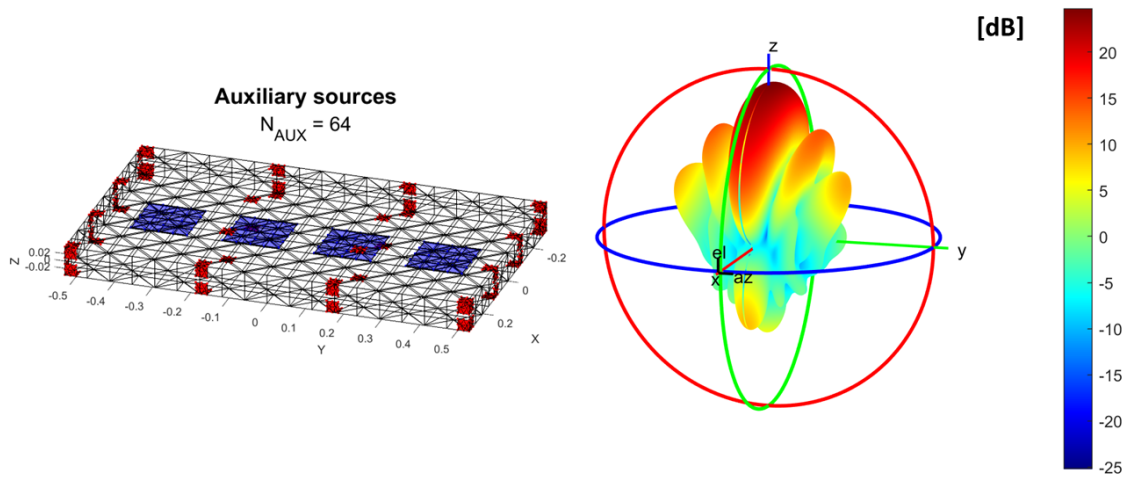


Figure 4.16. Distribution of 64 auxiliary sources around the linear array (left), FF pattern reconstructed (right).

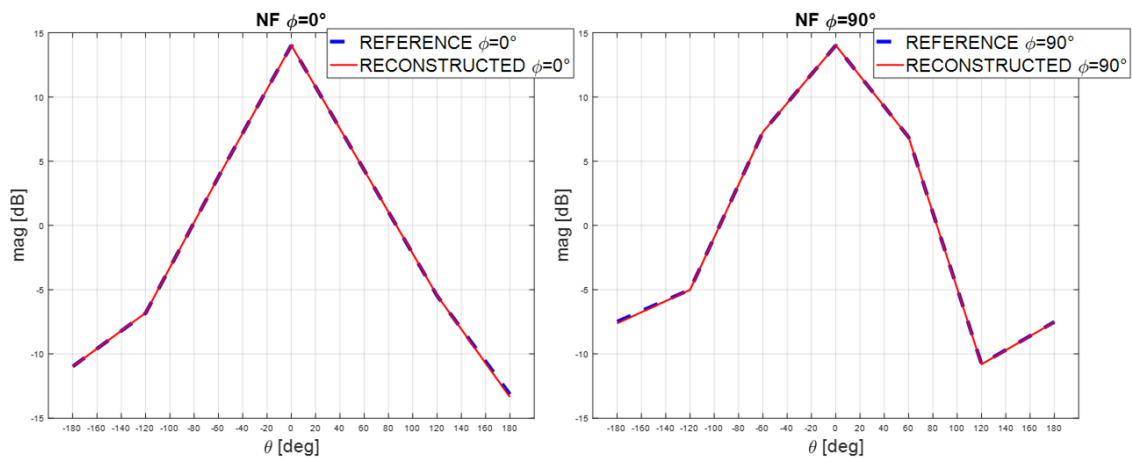


Figure 4.17. E-field NF reconstructed versus the reference E-field of the linear array for all the previous auxiliary source configurations.

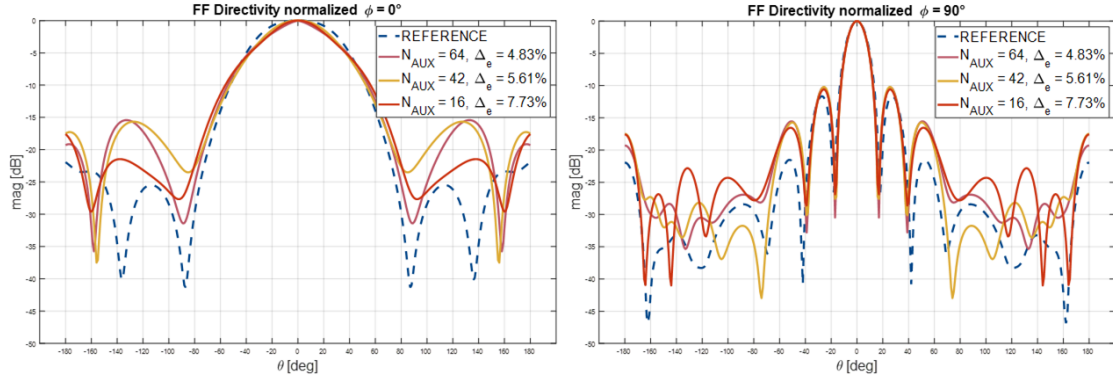


Figure 4.18. FF reconstructed normalized in directivity for each auxiliary source configurations with their relative reconstruction error.

To have a better understanding of the results just presented, it can be useful to compare them with the reconstruction of the linear array antenna by applying the inverse source on a reconstruction surface containing all the array, Figure 4.19, and with the reconstruction by using only the auxiliary sources, hence without the four elements translated, Figure 4.20.

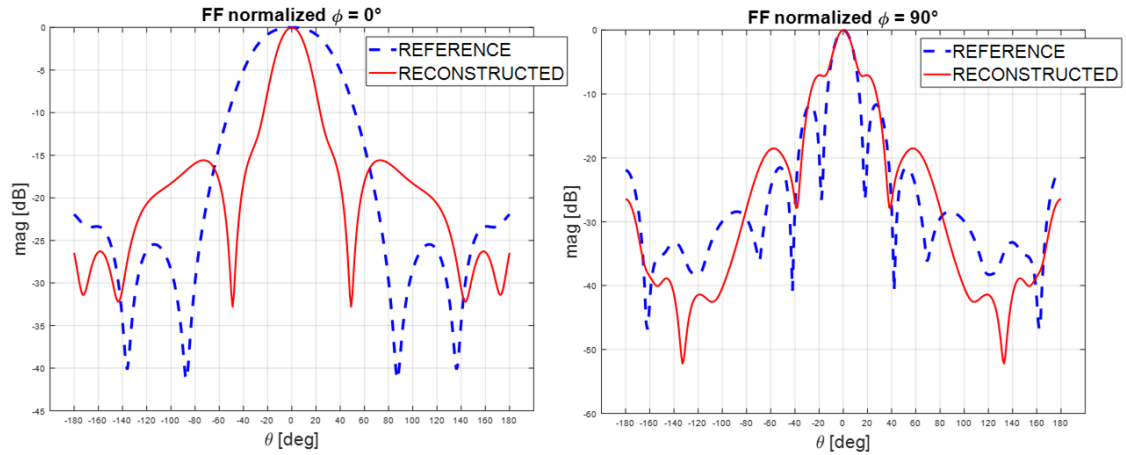


Figure 4.19. FF reconstruction with inverse-source of the linear array using 28 sampled points.

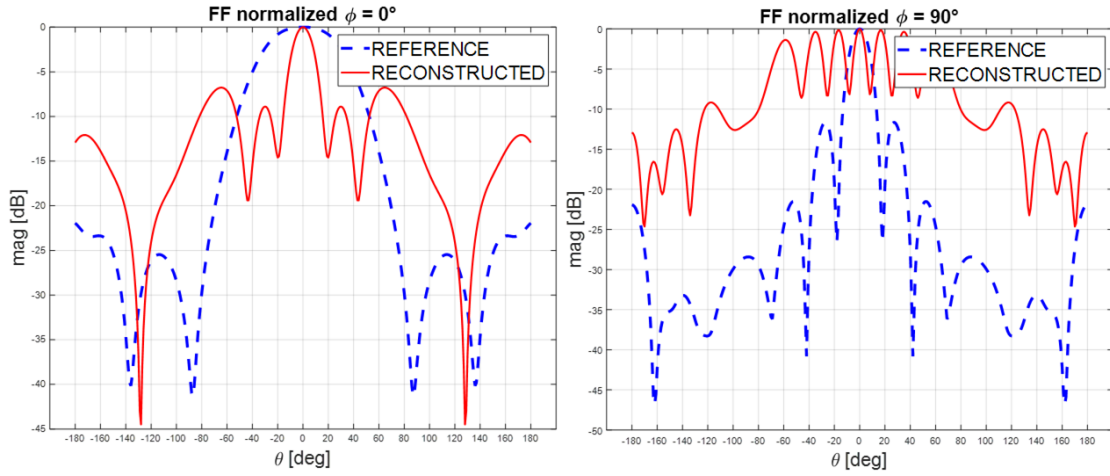


Figure 4.20. FF reconstruction of the linear array considering only the information from the auxiliary sources.

Table 4.5 reports the previous method's reconstruction errors.

inverse-source	$\Delta_e = 6.24\%$
Σ_R translation	$\Delta_e = 14.73\%$
Σ_R translation + 42 AUX sources	$\Delta_e = 5.61\%$

Table 4.5. Reconstruction errors results at 28 sampled points of all three reconstruction methods.

4.3 Reconstruction with 190 points

Now as a comparison with the previous results, it will be exploited the reconstruction of the linear array by using the minimum number of points needed for the characterization of the full array FF (i.e. 190 samples¹). It is expected that the reconstruction error of the single patch and the linear array will be lower with respect to the under-sampled case (28 points). In Figure 4.21 and Figure 4.22 is reported the reconstructed E-field in NF and FF of the single patch antenna with a reconstruction error of 0.42% in NF and 2.31% in FF.

¹The number of minimum sampled points is actually 177 but with the sampler, in CST the nearest sampling value was 190.

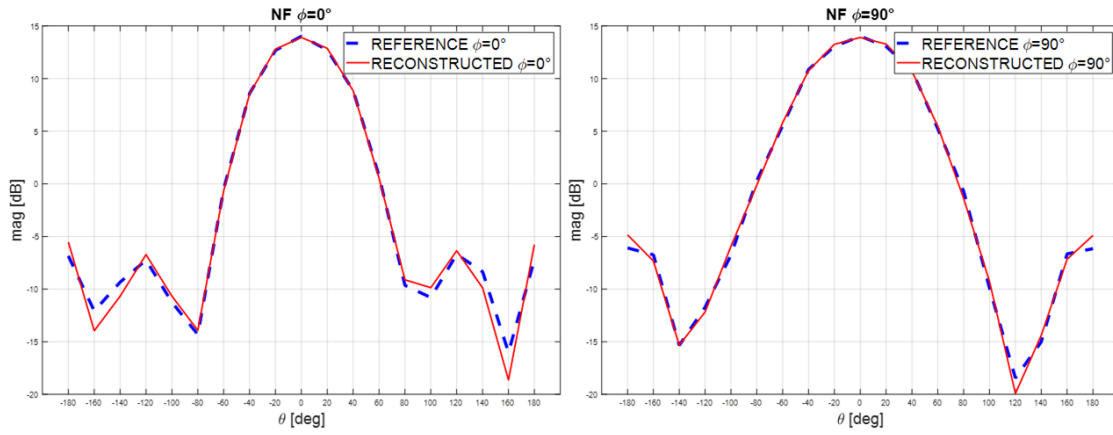


Figure 4.21. NF reconstructed (red) and NF reference (blue) of the single patch using 190 sampled points.

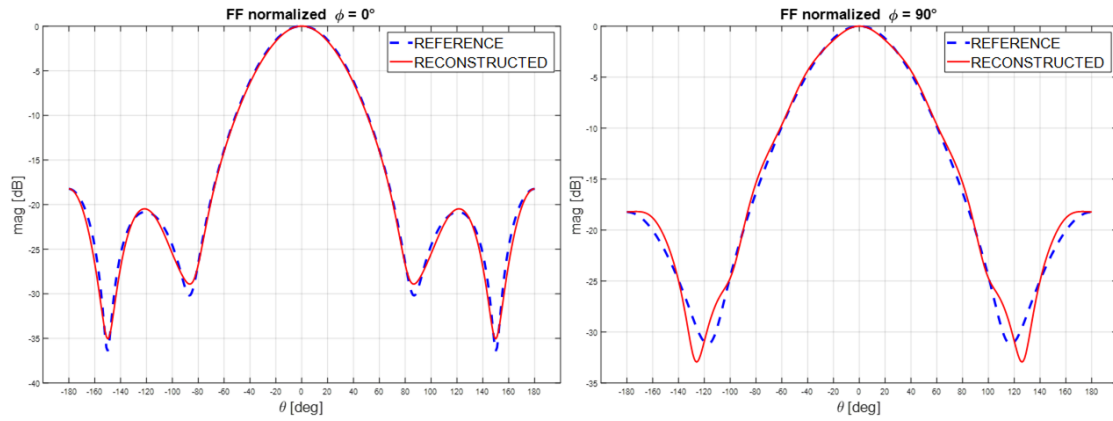


Figure 4.22. FF reconstructed (red) and FF reference (blue) of the single patch using 190 sampled points.

Using the same method as the previous section the reconstructed FF of the full array is presented and put in comparison with the other two methods.

- 1 - Inverse-source

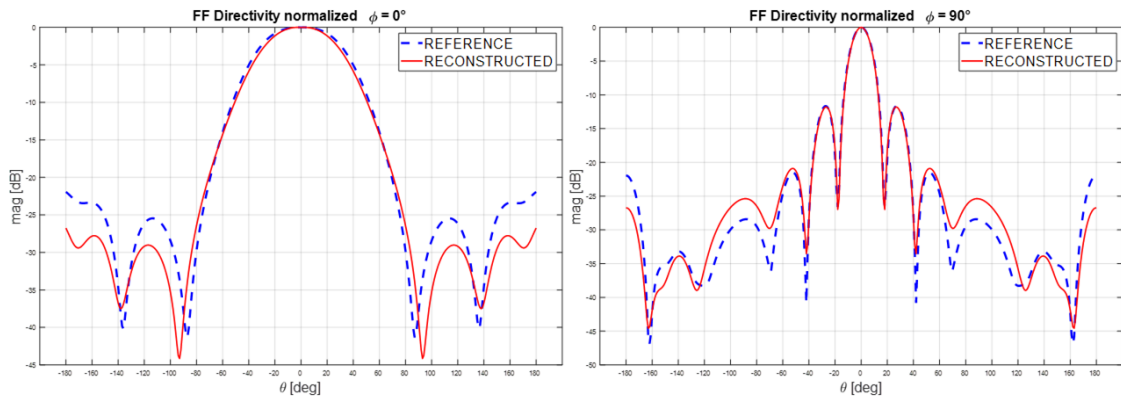


Figure 4.23. FF reconstruction normalize in directivity from applying the inverse-source to all the array structure.

- 2 - Σ_R translation

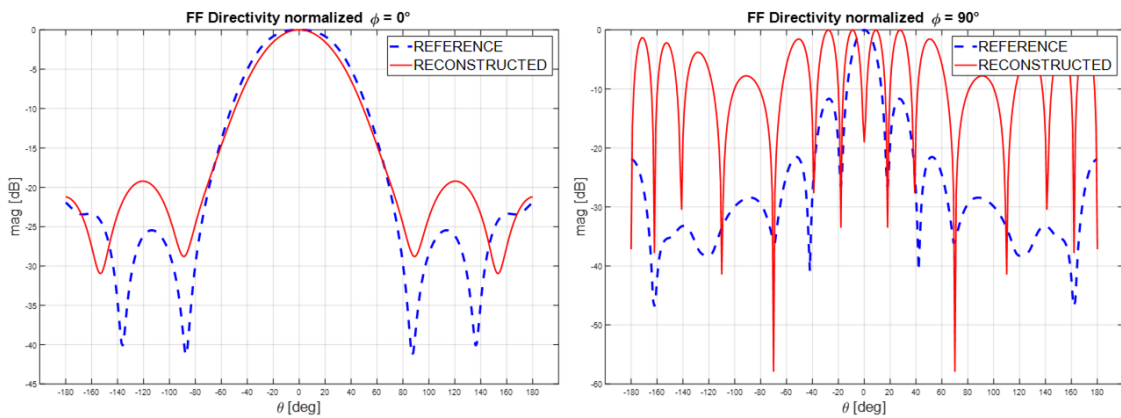


Figure 4.24. FF reconstruction normalize in directivity from translation of the reconstruction surface in each array element position, using the coefficients evaluated from the single element.

- **3 - Σ_R translation + auxiliary sources**

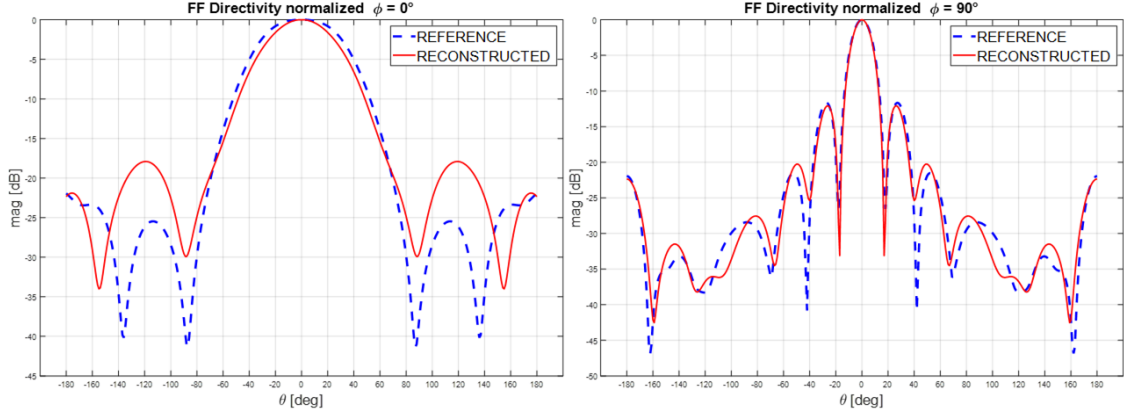


Figure 4.25. FF reconstruction normalize in directivity using the translating element and auxiliary sources.

From Table 4.6, where there are reported the previous results with their reconstruction errors, as was expected, it can be seen that by increasing the sampled points the reconstruction error of method 1. and method 3., both decreases.

	28 points	190 points
inverse-source	$\Delta_e = 49.6\%$	$\Delta_e = 6.24\%$
Σ_R translation	$\Delta_e = 14.73\%$	$\Delta_e = 11.81\%$
Σ_R translation + 42 AUX sources	$\Delta_e = 5.61\%$	$\Delta_e = 4.69\%$

Table 4.6. Reconstruction errors results between 28 and 190 sampled points.

4.3.1 Reconstruction with only auxiliary sources

The reconstruction process discussed in this thesis exploits the repetition design geometry of array antennas, compensating the missing information and making the equivalence currents radiate in all the other elements by translating the reconstruction surface. Even though this reconstruction method does not succeed, the information extrapolation from it was added to the auxiliary sources information to perform a better result. Therefore it should be questioned whether or not the first information (i.e. the one from the translation of reconstruction surfaces) is even necessary. So it was performed a reconstruction of the same linear array radiation pattern with the inverse-source technique was applied to a

single auxiliary source and then translated in each position to reconstruct the array FF. The results are shown in Figure 4.26 and demonstrate that the information derived from the array elements cannot be neglected.

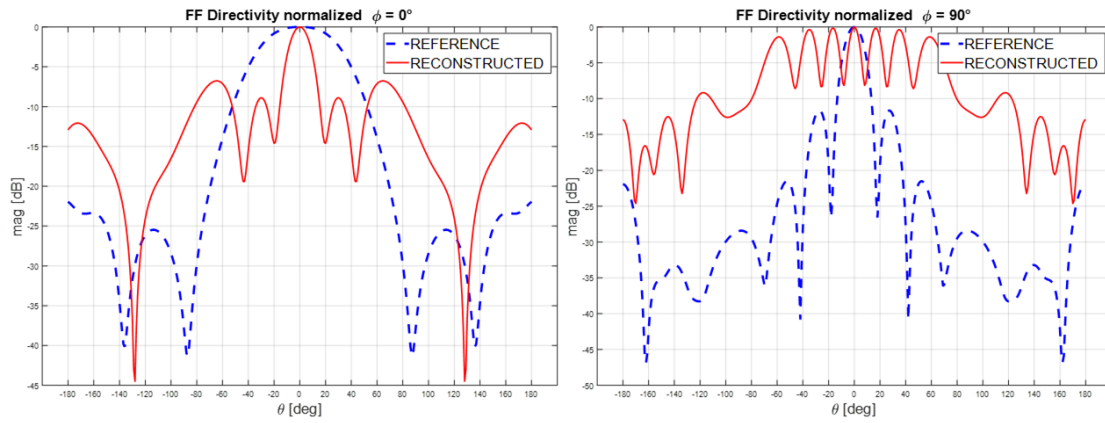


Figure 4.26. FF reconstruction normalize in directivity using only auxiliary sources (28 sampled points).

Chapter 5

Conclusion

Array antennas are complex structures created by arranging nearly identical antennas in an array (e.g., same geometry and same electromagnetic characteristics). An antenna radiation pattern could be reconstructed with a smaller number of samples by compensating for the missing information with a-priori knowledge derived from the single element theoretical characteristics. The reduction of sampling points for fast antenna measurements represents a great time reduction and, consequently, a cost-efficient alternative, even with a small percentage of error. In fact for the antenna characterization during the fabrication and test procedure, could be sufficient for the evaluation of the main lobe, second levels lobe (SLL) and eventually the back lobe.

The reconstruction of a 1GHz linear array FF with a relative reconstruction error of 5.61% was obtained after a simulation of ≈ 4.48 hours performed on a workstation with a CPU Intel Xenon at 2 GHz, 2 core and 192 GB of RAM. This result, compared to the reconstruction of the linear array FF using 190 samples with 6.24% of reconstruction error, shows a possible application (at least theoretical) for a new method of fast-antenna testing at NF. In Figure 5.2 is presented the reconstruction method with different sampled points between 28 and 190, with fixed amount of auxiliary sources, $N_{AUX} = 16$. It is noticeable how the reconstruction error sharply decreases with an increasing number of points.

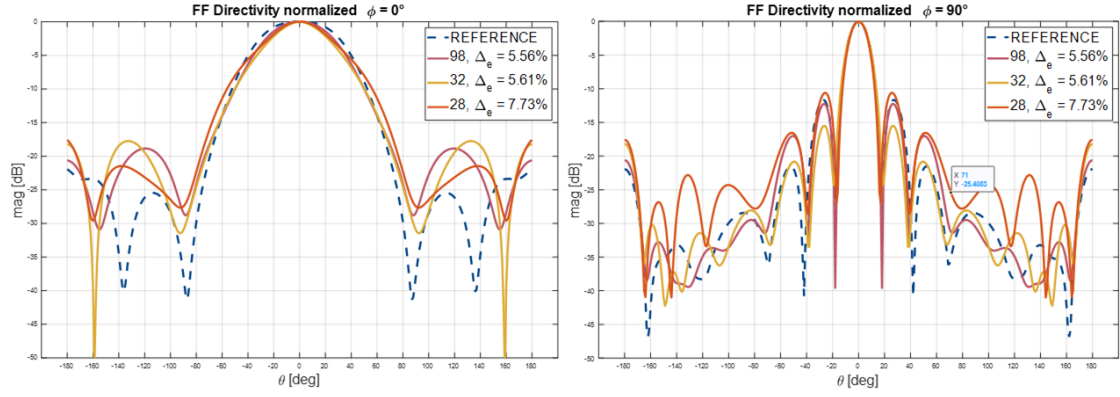


Figure 5.1. FF reconstruction normalize in directivity for 28, 32 and 98 sampled points with their relative reconstruction error, using 16 auxiliary sources.

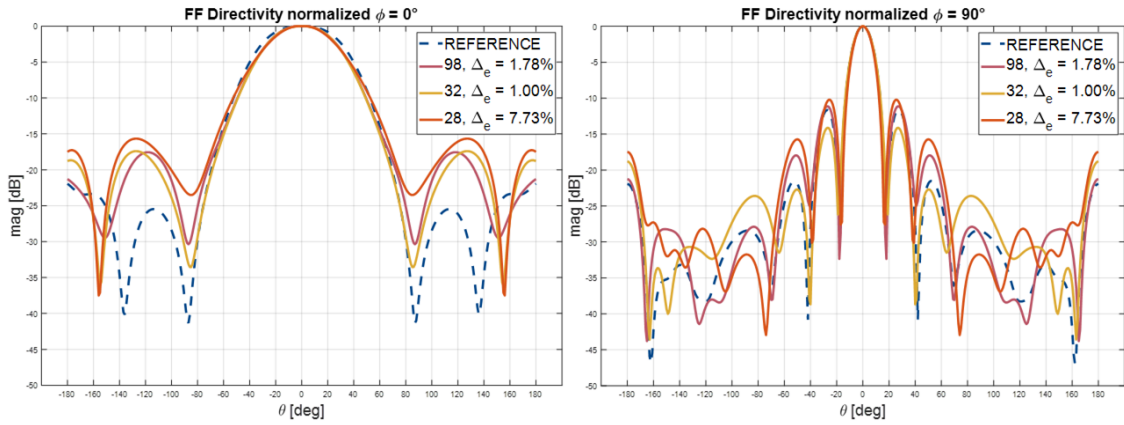


Figure 5.2. FF reconstruction normalize in directivity for 28, 32 and 98 sampled points with their relative reconstruction error, using 42 auxiliary sources.

In the design and prefabrication process of a complex antenna array, this method could ease the measurement setup and time giving an arbitrary approximation of the prototype characteristics in FF. The final result is presented in Figure 5.3 comparing the standard method for antenna measurement (inverse-source with 190 sampled points), and the new

method discussed in this thesis: the reconstruction translating the reconstruction surfaces of the single element sampled at 28 points, plus the auxiliary sources.

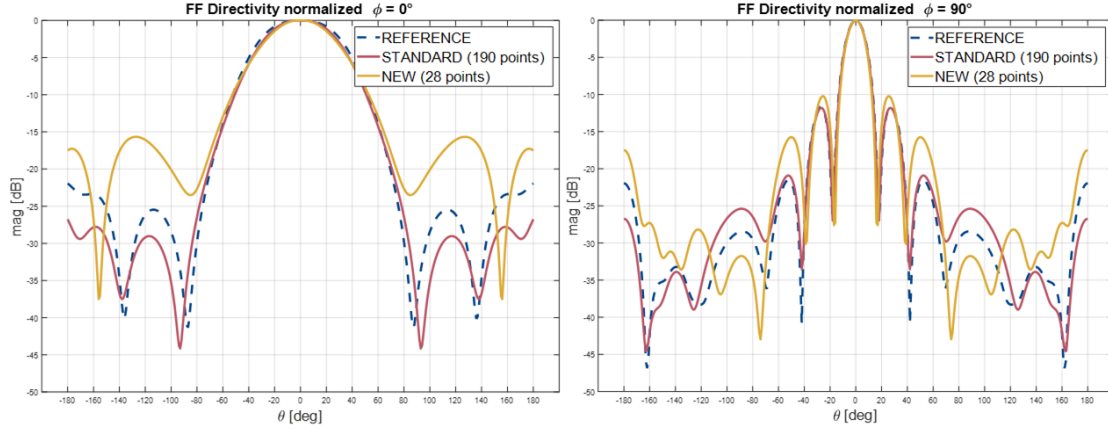


Figure 5.3. FF reconstruction normalize in directivity comparing the standard method with the new one proposed in this thesis.

5.0.1 Research limitations

A few limitations should be enlightened from the antenna simulations on which this work was based and the reconstruction process itself. Starting from the former, the simulated antenna materials were mainly idealistic such as the microstrip patch antenna substrate, vacuum with $\epsilon_r = 1$ and the metal patch modelled as PEC (Perfect Electric Conductor). Although this could affect only the first part of the process, hence the single element FF reconstruction error. The reconstruction process for the full array still stands itself. As the sampled points used for the NF reconstruction, these were extrapolated directly from CST Studio using its Post-Processing toolbox which automatically calculates the sample positions given a sampling step size. That it is not always accurate, in fact with the possibility to arbitrary select the best samples positions the reconstruction error in FF could be even smaller, leading to a better array reconstruction. Finally, for future research, it would be necessary to improve the auxiliary source distribution by minimizing the basis function number to optimize the computation.

Nevertheless, the feasibility of this process was demonstrated at a theoretical level and the possibility of future adjustments could lead to a better measurement solution for fast-antenna testing.

Appendix A

A.1 Surface Equivalence Principle Review

In electromagnetism, the surface equivalence principle or surface equivalence theorem relates to an arbitrary current distribution within an imaginary closed surface with an equivalent source on the surface. It is also known as the field equivalence principle, Huygens' equivalence principle or simply as the equivalence principle. Being a more rigorous reformulation of the *HuygensFresnel* principle, it is often used to simplify the analysis of radiating structures such as antennas. The equivalence principle is depicted in Figure A.1.

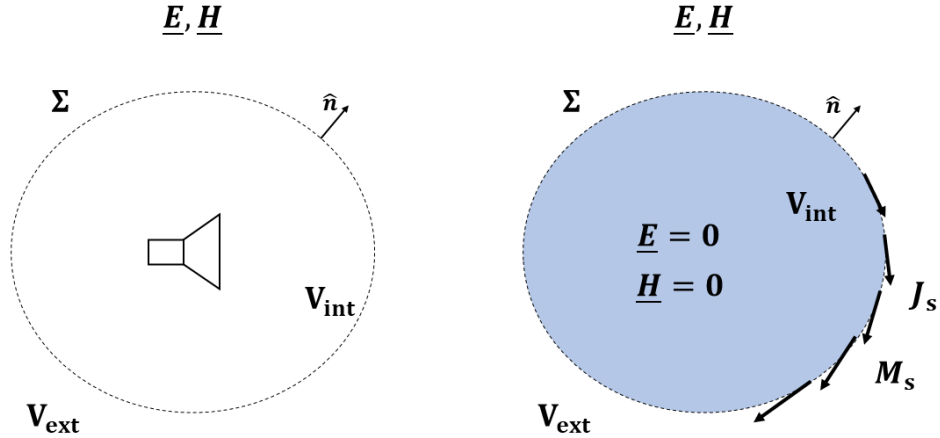


Figure A.1. Surface equivalence principle representation.

Expressing the exterior fields as V_{ext} and the interior fields as V_{int} , the following equations stand:

$$V_{int} + V_{ext}, \quad \begin{cases} -\nabla \times \underline{E} = j\omega\mu\underline{H} \\ \nabla \times \underline{H} = j\omega\epsilon\underline{E} + J_{src} \end{cases} \quad (\text{A.1})$$

$$\text{only } V_{ext}, \quad \begin{cases} -\nabla \times \underline{E} = j\omega\mu\underline{H} + \delta(P - P_{\Sigma})(\underline{E} \times \hat{n})|_{\Sigma} \\ \nabla \times \underline{H} = j\omega\epsilon\underline{E} + J_{src} + \delta(P - P_{\Sigma})(\hat{n} \times \underline{H})|_{\Sigma} \end{cases} \quad (\text{A.2})$$

Certain formulations of the principle are also known as Love equivalence principle and Schelkunoff equivalence principle, after Augustus Edward Hough Love and Sergei Alexander Schelkunoff, respectively. From the equation in A.2 it can be formulated the equivalent surface electric current A.3, and equivalent surface magnetic current A.4.

$$\underline{J}_S = (\hat{n} \times \underline{H})|_{\Sigma} \quad [A/m] \quad (\text{A.3})$$

$$\underline{M}_S = (\underline{E} \times \hat{n})|_{\Sigma} \quad [V/m] \quad (\text{A.4})$$

A.2 The Least Square Method

A least-square method is an approach to approximate the solution of a system of equations in which there are more equations than unknowns, by minimizing the sum of the square of the residuals from the results of each individual's equation. The objective is to adjust the parameters of a model function $f(x, \beta)$ to best fit a set of data.

The goal is to find the parameter m that best fits the data. The fit of a model is measured by its residual r , which is defined as the difference between the value predicted from the model and the observed value of the dependent variable.

$$r_i = y_i - f(x_i, \beta) \quad (\text{A.5})$$

Minimizing the sum S of the squared residual, the least-squares method finds the optimal values.

$$S = \sum_{i=1}^N r_i^2 \quad (\text{A.6})$$

A.3 Time domain solver overview

A time-domain solver calculates the development of electromagnetic fields through time at discrete locations and discrete-time samples. In CST Studio Suite there are available two high frequency time domain solvers: **Finite Integration Technique (FIT)**, called *Transient Solver*, and the one based on **Transmission Line Method (TLM)**, referred to as *TLM Solver*. Both solvers work on hexahedral mesh grids.

Transient Solver

The Transient Solver is based on the Finite Integration Technique, and it calculates the fields step by step in time by exploiting the Leap-Frog updating scheme. The value of the maximum usable time step is related to the minimum mesh step used in the definition of the problem's mesh. This implies that the higher the mesh resolution of one small detail, the higher the total simulation time.

The Finite Integration Technique (FIT)

The Finite Integration Technique is a numerical method first proposed by Weiland in 1976/1977 which provides a universal spatial discretization scheme that can be applied to various electromagnetic problems in the time or frequency domain.

Bibliography

- [1] *On the Solution of Inverse Equivalent Surface-Source Problems*, Jonas Kornprobst, Raimund A. M. Mauermayer, Ole Neitz, Josef Knapp, and Thomas F. Eibert, Progress In Electromagnetics Research, Vol. 165, 4765, 2019.
- [2] *Antenna Theory: Analysis and Design*, 3rd edition, Balanis, C.A., Wiley-Interscience, Apr. 2005.
- [3] *Field and Source Equivalence in Source Reconstruction on 3D Surfaces*, J. L. Araque Quijano and G. Vecchi, Progress In Electromagnetics Research, PIER 103, Vol. 67100, 2010.
- [4] *Fast Antenna Testing With Reduced Near Field Sampling*, Giorgio Giordanengo, Marco Righero, Francesca Vipiana, Giuseppe Vecchi, and Marco Sabbadini, IEEE Transactions on Antennas and Propagation, Vol. 62, No. 5, May 2014.
- [5] *Electromagnetic Scattering by Surfaces of Arbitrary Shape*, Sadasiva M. Rao, Donald R. Wilton, senior member, IEEE, and Allen W. Glisson, member IEEE.
- [6] *CST Studio Suite documentation*
- [7] *Antenna Characterization From a Small Number of Far-Field Measurements via Reduced-Order Models*, Nicolas Mézières , Michael Mattes , and Benjamin Fuchs , Senior Member, IEEE.
- [8] *Theory and Practice of Modern Antenna Range Measurements*, Parini, C., S. F. Gregson, J. McCormick, and D. J. V. Rensburg, The Institution of Engineering and Technology, London, UK 2014.